POLITECNICO DI TORINO

Master's Degree in Aerospace Engineering

Master's Degree Thesis

Fracture Resistance of Al2050 Alloy: Experimental Validation of Fracture Mechanics Models

Supervisors:
Prof. Giacomo Frulla
Prof. Thomas Pardoen
Sara Javangorouh

Author:
Andrea Del Giudice

June 2025

UCLouvain

Declaration of Research Location and Supervision

This Master's thesis was entirely carried out at the **Université catholique de Louvain (UCLouvain)**, in Belgium, within the research facilities of the Institute of Mechanics, Materials and Civil Engineering (iMMC). The full experimental campaign and all related analyses were conducted during an extended research stay from March to June 2025, hosted by the university and carried out under the supervision and scientific guidance of Prof. Thomas Pardoen and his team.

All laboratory work was performed using UCLouvain's advanced infrastructure, which includes high-precision mechanical testing machines, X-ray computed tomography equipment, 3D optical and scanning electron microscopes, and specimen preparation systems such as cutting and polishing machines. The research also benefited from the technical support and expertise of the laboratory staff, ensuring that all procedures were performed following rigorous academic and scientific standards.

The Al2050 material used in this work was supplied by an industrial partner and its usage was coordinated and approved by UCLouvain in compliance with the objectives of the ongoing research activities at the host institution. The integration of this material into the study was facilitated through the collaboration with the HAPI (Hutchinson–Atkins–Pineau Initiative) research project, funded by the European Research Council (ERC), to which UCLouvain actively contributes.

All experimental data, interpretations, and scientific discussions presented in this thesis were first reviewed and validated internally by the academic staff at UCLouvain, ensuring compliance with their institutional requirements for research quality and methodology. Subsequently, the thesis was also reviewed, approved, and accepted by the academic board of the **Politecnico di Torino**, in accordance with the standards and regulations of the Master's Degree Programme in Aerospace Engineering.

This collaborative framework between UCLouvain and Politecnico di Torino provided a valuable international research environment, which significantly enriched the academic and technical development of the work. The support, resources, and expertise offered by UCLouvain were instrumental to the successful completion of this thesis.

Louvain-la-Neuve, Belgium
June 2025

Abstract

The fracture toughness of a material is a critical factor in structural design and in the material selection process, as it ensures safe and reliable results. This Master's thesis investigates the effect of thickness on the fracture toughness of Al2050 aluminum-copper alloy, a material widely used in aerospace and automotive industries due to its lightweight and high-strength properties. The study aims to identify the optimal thickness that maximizes fracture resistance while maintaining mechanical performance. Double Edge Notched Tensile (DENT) specimens of varying thicknesses were tested under controlled conditions to evaluate fracture toughness using the Essential Work of Fracture (EWF) methodology.

The results reveal a significant thickness dependence, with thinner sheets exhibiting higher fracture toughness due to plane stress dominance, while thicker sheets show reduced toughness under plane strain conditions. However, while fracture resistance is a key parameter for structural integrity, material selection in engineering applications often involves trade-offs with other mechanical properties, such as tensile strength, fatigue resistance, or weight savings. The findings of this study provide practical guidelines for balancing these competing factors, contributing to the development of lightweight, high-performance structures. This research bridges the gap between material science and industrial applications, offering insights for the design of next-generation materials.

Contents

1 Introduction 10
1.1 Context and Motivation 10

2 Theoretical Background 13
2.1 Fundamentals of Fracture Mechanics 13
2.1.1 Energy-Based Approach to Fracture 15
2.2 Factors Affecting Fracture Toughness 18
2.2.1 Effect of Strain Hardening 19
2.2.2 Influence of Thickness 21
2.3 Mechanisms of Fracture in Metallic Materials 22
2.3.1 Ductile vs. Brittle Fracture 22
2.4 Physics of ductile fracture 24
2.4.1 Crack Tip Plasticity and Small Scale Yielding (SSY) 24
2.4.2 Elasto-Plastic Fracture Mechanics (EPFM) 25
2.4.3 Crack Tip Opening Displacement (CTOD) 26
2.4.4 Essential Work of Fracture (EWF) 28
2.5 X-ray Computed Tomography 29
2.5.1 Principles of X-ray Attenuation and Reconstruction 29
2.5.2 Applications to Fracture Analysis of Al2050 30

3 Material Characterisation and Experimental Procedures 31
3.1 Aluminum 2050 T3 33
3.1.1 Elemental composition of Al2050 T3 33
3.1.2 Homogeneity through the thickness 33
3.1.3 Chemical Etching of Al2050-T3 Alloy 36
3.1.4 Microstructural Observation and Results 36
3.2 Crack Tip Opening Displacement (CTOD) Experiments on Al2050 T-8 Alloy 41
3.2.1 Fatigue Pre-Cracking 41
3.2.2 CTOD Testing Procedure 44
3.3 Comparison between Al2050-T3 and Al2050-T8 Conditions 46

4 Experimental Results and Discussion 47
4.1 Mechanical Testing results 47
4.2 Fractographic Examination 50
4.3 CTOD Test Results 55
4.4 X-ray Computed Tomography Results 60

4.4.1 Destructive Through-Thickness Crack Characterization via Stepwise Polishing 64

5 Conclusions **66**

A Preliminary CTOD Tests on Al2050-T3 **72**

A.1 Crack Tip Opening Displacement (CTOD) Experiments on Al2050 T-3 Alloy 72

A.1.1 Fatigue Pre-Cracking 73

List of Figures

1.1.1 Ashby material selection chart, Fracture toughness as a function of yield strength [1] 11

2.1.1 Stress concentration around an elliptical hole in a plate in tension [2] . 14
2.1.2 The three fundamental modes of crack propagation [3] 17
2.2.1 Stress-strain curve for a ductile material, highlighting strain hardening and necking [4] 21
2.2.2 Dependence of fracture toughness on thickness of the specimen [5] . . . 22
2.3.1 Micro-mechanical steps of ductile fracture [6]. 23
2.3.2 Stress-strain curves for a ductile material and a brittle material 24
2.4.1 Definition of the J -integral contour [7] 26
2.4.2 Determination of Crack Tip Opening Displacement (CTOD) [8] 27
2.5.1 Schematic illustration of the working principle of micro CT [9] 29

3.1.1 Part of the drawings provided to Constellium 33
3.1.2 Schematic representation of the Vickers hardness test [10] 34
3.1.3 Microhardness profiles through thickness for (a) rolling direction and (b) transverse direction specimens 35
3.1.4 RD sample at 400× magnification showing grain structure after Keller's etching 37
3.1.5 TD sample at 400× magnification showing grain structure after Keller's etching 38
3.1.6 TD sample used for observations, highlighting the three areas: 1 left, 2 middle, 3 right 39
3.1.7 SEM images through the thickness of the Al2050 plate (RD) 39
3.1.8 SEM images through the thickness of the Al2050 plate (TD) 40
3.2.1 Geometry of the Al2050 T-3 specimen 42
3.2.2 3D microscope images showing crack features for 1 mm thick sample . . 43
3.2.3 3D microscope images showing crack features for 10 mm thick sample . 44
3.2.4 Schematic of crack tip evolution during CTOD test: δ_1, δ_2, and Δa [11]. 45
3.2.5 : Schematic of the plot used in multiple specimen method for determining the unloaded plastic CTOD [11]. 45

4.1.1 Geometry dimensions of the flat dog-bone tensile specimen (thickness: 1mm) 47
4.1.2 Engineering (a) and True (b) stress-strain curves for Al2050-T3 specimens tested in rolling direction (RD) and transverse direction (TD). . . 48

4.2.1 Logarithmic representation of force versus displacement for fractured DENT specimens with thickness of 1 mm and 10 mm 51
4.2.2 Fracture surface of the ligament area of 1mm thick sample 52
4.2.3 (a) SEM reconstructed image of the 1mm sample, (b) Fatigue Pre-Crack Zone, (c) Triangular Stable Growth Zone, (d) Slant Fracture Zone . . 53
4.2.4 Fracture surface of the ligament area of 10mm thick sample 54
4.2.5 (a) SEM reconstructed image of the 10mm sample, (b) Fatigue Pre-Crack Zone, (c) Central flat crack region, (d) Surface slant crack zone 55
4.3.1 Load-displacement curves for 1 mm thick DENT specimens 57
4.3.2 Load-displacement curves for 2 mm thick DENT specimens 57
4.3.3 Load-displacement curves for 4 mm thick DENT specimens 58
4.3.4 Load-displacement curves for 10 mm thick DENT specimens 58
4.4.1 Comparative X-ray tomography images of 10 mm thick specimen showing through-thickness crack progression differences 60
4.4.2 Δa through the thickness of samples with thickness of 1 mm 61
4.4.3 Δa through the thickness of samples with thickness of 2 mm 61
4.4.4 Δa through the thickness of samples with thickness of 4 mm 61
4.4.5 Δa through the thickness of samples with thickness of 10 mm 62
4.4.6 δ_1-δ_2 as a function of Δa 62
4.4.7 Comparison between crack length measured with tomography and polishing + 3D microscope for the same 4 mm sample 64
4.4.8 Comparison between crack length measured with tomography and polishing + 3D microscope for the same 10 mm sample 65

A.1.1Geometry of the Al2050 T-3 specimen 73
A.1.23D microscope images showing crack features for 2 mm thick sample . . 76
A.1.33D microscope images showing crack features for 4 mm thick sample . . 77

List of Tables

3.1.1 Elemental composition of Al2050 T3 (%wt) obtained by ICP analysis. . 34
3.1.2 Chemical composition of the Keller's reagent used for etching [12] . . . 36
3.2.1 Average fatigue pre-crack parameters of the samples 42
3.2.2 Averaged dimensions of the T-8 samples after fatigue pre-cracking . . . 43

4.1.1 Averaged mechanical properties of Al2050-T3 in rolling direction (RD) and transverse to rolling direction (TD). The values represent the mean of two tested specimens for each orientation. 49
4.1.2 Averaged hardening law parameters for Al2050-T3 50
4.2.1 Maximum force and displacement values 51
4.3.1 Peak load and displacement values for 1 mm thick samples 55
4.3.2 Peak load and displacement values for 2 mm thick samples 56
4.3.3 Peak load and displacement values for 4 mm thick samples 56
4.3.4 Peak load and displacement values for 10 mm thick samples 56
4.4.1 Critical CTOD δ_c values for each specimen thickness, obtained by linear regression at $\Delta a = 0$ 63

A.1.1atigue pre-cracking parameters for 4 mm specimens 73
A.1.2Fatigue pre-cracking parameters for 2 mm specimens 74
A.1.3Fatigue pre-cracking parameters for 1 mm specimens 75
A.1.4Averaged dimensions of the 2 mm T-3 samples after fatigue pre-cracking 75
A.1.5Averaged dimensions of the 4 mm T-3 samples after fatigue pre-cracking 75

Table of Symbols

Latin Symbols

Symbol	Description	Units
A	Stress amplitude in Swift hardening law	MPa
a	Crack length	mm
a_0	Initial notch length	mm
A_0	Initial cross-sectional area	mm^2
B	Thickness of the specimen	mm
E	Young's modulus	MPa
F	Applied load	N
$F_{\max}$	Maximum force during fatigue loading	N
$F_{\min}$	Minimum force during fatigue loading	N
G	Strain energy release rate	J/m^2
G_c	Critical strain energy release rate (fracture energy)	J/m^2
G_s	Surface energy per unit area	J/m^2
G_p	Plastic energy dissipation	J/m^2
J	J-integral (path-independent energy release rate)	J/m^2
K	Stress intensity factor (SIF)	MPa$\cdot\sqrt{\text{mm}}$
K_I	Mode I stress intensity factor	MPa$\cdot\sqrt{\text{mm}}$
K_{IC}	Fracture toughness under plane strain conditions	MPa$\cdot\sqrt{\text{mm}}$
L_0	Original gauge length of the tensile specimen	mm
N_i	Number of fatigue cycles at load F_i	–
n	Hardening exponent in Swift hardening law	–
r_p	Plastic zone radius at the crack tip	mm
T_i	Traction components used in J-integral	N
u_i	Displacement components in J-integral	mm
W	Strain energy density	MPa

Greek Symbols

Symbol	Description	Units
α	Angle (used implicitly in stress concentration contexts)	rad or °
δ	Crack Tip Opening Displacement (CTOD)	mm
δ_1	Total crack tip opening after blunting	mm
δ_2	Tearing crack tip opening	mm
Δa	Crack extension during tearing	mm
ϵ	Engineering strain	–
ϵ_p	Plastic strain	–
ϵ_0	Offset strain parameter in Swift law	–
ϵ_{eng}	Engineering strain	–
ϵ_{true}	True strain	–
σ	True stress	MPa
σ_{eng}	Engineering stress	MPa
σ_{true}	True stress	MPa
σ_Y	Yield strength	MPa
Γ	Integration contour for J-integral	–
σ_{ij}	Stress tensor component used in HRR field	MPa

Chapter 1

Introduction

1.1 Context and Motivation

The quest for lightweight yet durable materials has driven significant advancements in material science, particularly in the development of high-performance aluminum alloys. Among these, **Al2050**, an aluminum-lithium (Al-Li) alloy, has garnered considerable attention due to its exceptional combination of low density, high stiffness, and excellent fatigue resistance. These properties make Al2050 a prime candidate for applications in industries such as aerospace and automotive, where weight reduction is critical for improving fuel efficiency and performance.

The **thickness** of a material is a crucial factor influencing its mechanical behavior, particularly its **fracture toughness (FT)**. Fracture toughness, which measures a material's resistance to crack propagation, is highly dependent on the stress state near the crack tip. In thin sheets, the stress state is typically dominated by **plane stress** conditions, leading to a larger plastic zone and higher energy dissipation during fracture. In contrast, thicker materials exhibit **plane strain** conditions, resulting in a smaller plastic zone and lower fracture toughness. This thickness dependence presents a fundamental challenge for material selection, as standard material selection tools like **Ashby charts** [13] primarily report the plane strain fracture toughness (K_{Ic}) measured at greater thicknesses. These charts, while invaluable for comparing material performance, overlook a critical phenomenon: fracture toughness under plane stress conditions (typical of thin sheets) can exhibit a significant peak, potentially offering superior damage tolerance for lightweight designs. Understanding this thickness-dependent transition is therefore essential for optimizing structural components where both weight reduction and fracture resistance are paramount.

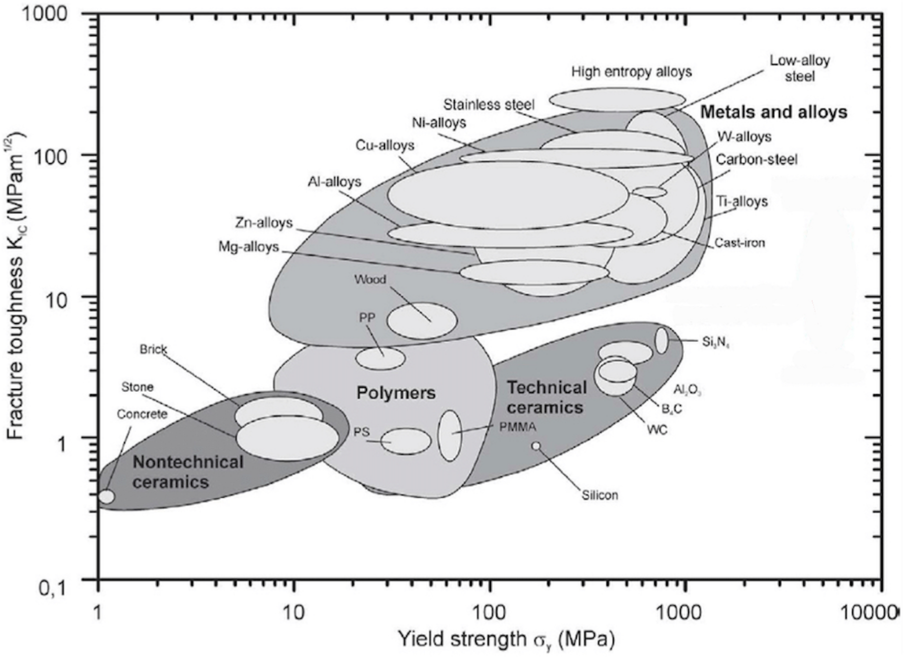

Figure 1.1.1: Ashby material selection chart, Fracture toughness as a function of yield strength [1]

The primary objective of this thesis is to investigate the **thickness effect on fracture toughness** in Al2050 aluminum alloy sheets. Specifically, the study aims to determine the **optimal thickness** that maximizes fracture resistance while maintaining other mechanical properties. This research is motivated by the need to develop lightweight materials that can withstand the demanding conditions of advanced engineering applications, such as aircraft fuselages and electric vehicle chassis.

To achieve this goal, the study will employ **Double Edge Notched Tensile (DENT)** specimens of varying thicknesses. The DENT configuration is particularly suitable for evaluating fracture toughness in thin sheets, as it allows for the precise control of crack initiation and propagation. In addition, the presence of two notches prevents out-of-plane deformation, ensuring that no buckling occurs during tensile testing, an essential condition for obtaining reliable fracture data in thin materials. By conducting a series of interrupted and fully fractured tests, this research aims to:

- **Quantify the thickness dependence of fracture toughness** in Al2050, focusing on the transition between plane stress and plane strain conditions.
- **Identify the optimal thickness** that balances weight reduction and fracture resistance, providing practical guidelines for material selection in engineering applications.

Fracture toughness will be assessed through **Crack Tip Opening Displacement (CTOD)** testing, a method particularly suited for characterizing ductile fracture in metallic materials. CTOD provides a direct measure of the crack tip deformation and serves as a reliable parameter to assess fracture resistance under varying constraint conditions. Experiments will be carried out on Al2050 samples with four distinct thicknesses: **1 mm**, **2 mm**, **4 mm**, and **10 mm**, covering a full spectrum from near plane stress to near plane strain conditions. This approach enables a comprehensive evaluation of how thickness influences the fracture behavior. Following the CTOD tests, **fractographic analyses** will be conducted on the fractured surfaces to investigate the micromechanisms of crack propagation and damage, providing insight into the underlying failure processes.

European Research Council
Established by the European Commission

This thesis contributes to a larger research effort led by UCLouvain and financed by the European Research Council (ERC), within the framework of the **HAPI** project (Hutchinson–Atkins–Pineau Initiative). The vision of the HAPI project is that the fracture resistance of metallic components can be significantly enhanced by selecting and/or controlling the optimum plate thickness in thin-walled structures and in the constituents of thick laminates. Positioned at the interface between solid mechanics and metallurgy, HAPI combines processing techniques, experimental investigation, and numerical simulations to achieve its objectives.

The findings of this research will contribute to the broader understanding of fracture mechanics in aluminum alloys and provide practical insights for the design of lightweight, high-performance structures. By identifying the optimal thickness for Al2050, this study aims to bridge the gap between material science and engineering applications, paving the way for the development of next-generation materials that meet the demands of modern technology.

Note on Material Selection

Although the initial objective of this thesis was to investigate the fracture behaviour of the Al2050-T3 alloy, due to unforeseen logistical and technical issues related to the availability and preparation of specimens, the main experimental campaign was ultimately carried out on Al2050-T8. The T3 condition was originally selected for its higher ductility and relevance to certain aerospace applications, but the delay in specimen preparation and quality control made it unsuitable for continued testing.

However, in this thesis, the material characterization work performed on Al2050-T3 is presented, including microstructural, chemical, and mechanical analysis, as it remains valuable in understanding the baseline properties of the alloy system and serves as a meaningful point of comparison to the T8 variant. Experimental fracture toughness tests (CTOD) were performed solely on the T8 condition, and these results form the core of the analysis and conclusions of this work.

Some preliminary CTOD data on Al2050-T3 were acquired before switching to T8; These are included in the Appendix A.1.1 for completeness, but are not used in the final performance assessment.

Chapter 2

Theoretical Background

2.1 Fundamentals of Fracture Mechanics

Fracture toughness is a fundamental property that defines a material's ability to resist crack propagation under applied stress. It plays a crucial role in the selection and design of structural materials, particularly in aerospace and mechanical engineering, where failure due to crack growth can lead to catastrophic consequences. The concept of fracture toughness originates from *Fracture Mechanics*, a field that provides a framework for understanding the behavior of materials containing pre-existing flaws and predicting their failure under different loading conditions [14].

Materials exhibit different fracture behaviors depending on their microstructure, loading conditions, and environmental factors. In general, materials can be categorized as **ductile** or **brittle**, based on their ability to undergo plastic deformation before failure. Ductile materials, such as most aluminum and steel alloys, absorb more energy before fracture, while brittle materials, such as ceramics or high-strength composites, tend to fail suddenly with minimal plastic deformation [15].

A key factor influencing fracture toughness is the *state of stress at the crack tip*, which depends on the specimen thickness. In **plane stress conditions** (typically in thin specimens), plastic deformation is more pronounced, leading to higher fracture toughness values. Conversely, in **plane strain conditions** (found in thicker specimens), plasticity is restricted, and fracture toughness reaches a lower limit, known as the *plane strain fracture toughness* K_{IC}, which is an intrinsic material property [16].

Understanding fracture toughness is essential for predicting failure, optimizing material selection, and improving structural integrity. The following sections will explore the fundamental aspects of fracture mechanics, including fracture criteria, plastic zone formation, crack propagation mechanisms, and experimental methods used to evaluate fracture toughness.

Crack Initiation Mechanisms

Crack formation can be attributed to various mechanisms, depending on material properties, loading conditions, and environmental factors.

- **Microstructural Inhomogeneities:** Internal defects such as inclusions, voids, and second-phase particles act as stress raisers and serve as nucleation sites for crack formation, particularly under cyclic loading [17].

- **Geometric Discontinuities:** Sharp corners, keyholes, and fillets in structural components cause localized stress concentration, increasing the risk of crack initiation. The severity of stress concentration depends on the notch radius r, with sharper notches leading to higher values of K_t [18].

- **Surface Defects and Corrosion:** Surface roughness, machining marks, and environmental corrosion introduce micro-cracks that grow under applied stresses. In aerospace applications, fatigue cracks frequently initiate from surface defects due to repeated loading cycles [19].

- **Plastic Deformation and Dislocation Pile-up:** In ductile materials, stress concentration leads to dislocation accumulation at barriers such as grain boundaries. When the local stress exceeds a critical value, micro-voids form and coalesce, leading to ductile crack propagation [20].

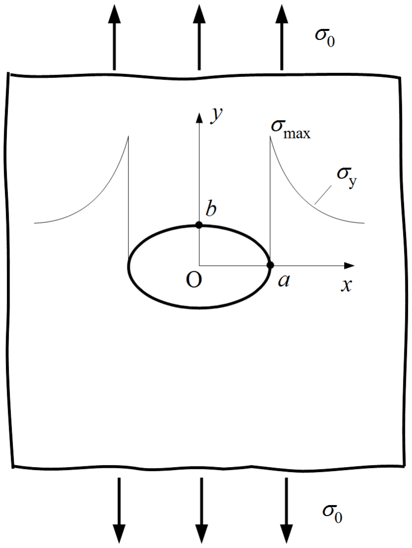

Figure 2.1.1: Stress concentration around an elliptical hole in a plate in tension [2]

Griffith's Theory of Crack Formation

A pioneering approach to understanding fracture was developed by Griffith (1921), who introduced an energy-based criterion for crack growth [21]. The total energy of a system containing a crack is given by:

$$U_{\text{total}} = U_{\text{elastic}} + U_{\text{surface}} \tag{2.1.1}$$

where:

- U_{elastic} represents the stored elastic strain energy.

- U_{surface} represents the energy required to create new surfaces.

Griffith's criterion states that a crack will propagate when the energy release rate G exceeds the critical energy release rate G_c:

$$G = \frac{\pi \sigma^2 a}{E} \geq G_c \tag{2.1.2}$$

where a is the crack length, E is Young's modulus, and σ is the applied stress.

Stress Fields Near a Crack Tip

Irwin (1957) extended Griffith's work by introducing the concept of the stress intensity factor K, which characterizes the stress field around a crack tip [22]:

$$\sigma_{ij} = \frac{K}{\sqrt{2\pi r}} f_{ij}(\theta) \tag{2.1.3}$$

where $f_{ij}(\theta)$ are functions describing the angular distribution of stress around the crack tip, and r is the radial distance from the crack tip.

2.1.1 Energy-Based Approach to Fracture

The study of fracture mechanics can be approached from both stress-based and energy-based perspectives. While stress concentration analysis provides insight into local failure conditions, an energy-based approach allows a more comprehensive understanding of fracture propagation by considering the global energy balance of a system. This method was pioneered by Griffith in 1920 and later extended to elastic-plastic materials by Irwin and Orowan [23–25].

Griffith's Energy Criterion

Griffith's theory of brittle fracture postulates that a crack propagates when the decrease in elastic strain energy is sufficient to overcome the surface energy required to create new crack surfaces. Mathematically, this criterion can be expressed as:

$$G = \frac{dU}{dA} \tag{2.1.4}$$

where:

- G is the strain energy release rate,
- U is the total elastic strain energy stored in the material,
- A is the crack area.

For a material with an initial crack of length a, Griffith derived the critical condition:

$$G_c = \frac{2\gamma_s}{E} \tag{2.1.5}$$

where:

- G_c is the critical energy release rate,

- γ_s is the surface energy per unit area,
- E is the Young's modulus of the material.

This formulation explains why brittle materials, such as glass, exhibit lower fracture toughness compared to ductile metals, as the latter dissipate energy through plastic deformation before fracture. Griffith's formulation assumes a linear elastic, isotropic, and homogeneous material with negligible plasticity at the crack tip, conditions generally satisfied in brittle materials.

Extension to Ductile Materials

While Griffith's theory accurately describes brittle fracture, ductile materials require an additional term to account for plastic work. Orowan and Irwin extended Griffith's theory by introducing a plastic dissipation term G_p, leading to:

$$G_c = G_s + G_p \tag{2.1.6}$$

where G_p represents the energy absorbed by plastic deformation at the crack tip. This concept is particularly relevant for metals like aluminum alloys, where a significant portion of the fracture energy is dissipated in plastic deformation before crack propagation occurs [26].

The Role of Thickness in Fracture Energy

As discussed in the previous section, stress concentration plays a critical role in crack initiation. However, when considering fracture propagation, the specimen thickness becomes a key factor. In thin specimens, plane-stress conditions prevail, allowing greater plastic deformation and higher energy dissipation. In contrast, thick specimens exhibit plane-strain conditions, where plasticity is constrained, leading to lower fracture toughness values. This effect is quantified through the critical stress intensity factor K_{IC}, which is related to G_c by:

$$K_{IC} = \sqrt{EG_c} \tag{2.1.7}$$

for plane-strain conditions. This relationship highlights the dependency of fracture resistance on both material properties and geometric constraints [27].

Stress Intensity Factor and Crack Driving Force

While the previous sections described how stress concentrates at discontinuities and how fracture can be analyzed from an energy perspective, the *Stress Intensity Factor* (SIF), denoted as K, provides a quantitative measure of the severity of the crack-tip stress field under different loading conditions, therefore it's a fundamental parameter used to characterize the stress field near a crack tip [24, 26].

Definition and Significance of the Stress Intensity Factor

The stress intensity factor K describes how an external load is transmitted to the crack tip and is defined by:

$$K = Y\sigma\sqrt{\pi a} \tag{2.1.8}$$

where:

- Y is a geometric correction factor that depends on specimen and crack geometry,
- σ is the applied stress,
- a is the crack length.

The SIF is crucial because it enables the prediction of crack propagation using fracture mechanics principles rather than empirical testing alone. It is particularly useful for designing damage-tolerant structures in aerospace and other high-performance applications [28].

Modes of Crack Loading

Cracks can experience different types of loading, each influencing the stress distribution around the crack tip:

1. **Mode I – Opening Mode**: The most common loading mode, where tensile stress is applied perpendicular to the crack faces, causing them to separate.
2. **Mode II – Shear Mode**: Shear stress is applied parallel to the crack plane, leading to in-plane sliding.
3. **Mode III – Tearing Mode**: Out-of-plane shear stress causes an anti-plane shear deformation.

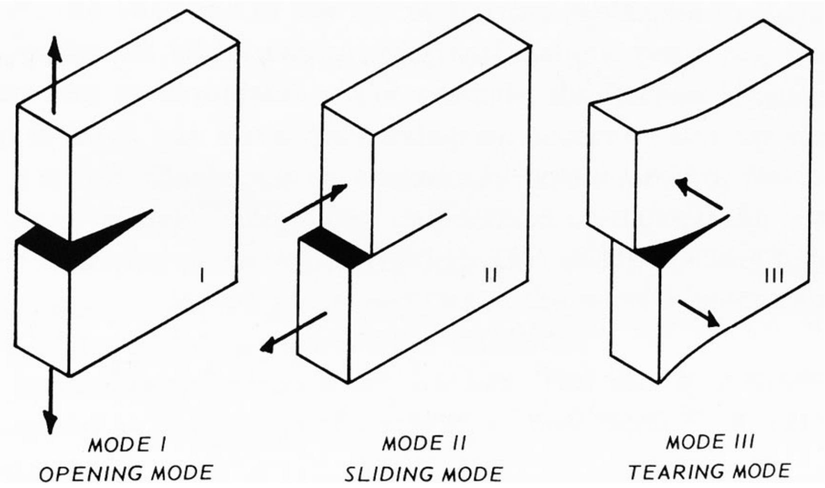

Figure 2.1.2: The three fundamental modes of crack propagation [3]

Crack Driving Force and Fracture Toughness

The concept of *crack driving force* describes the external energy available to propagate a crack. It is related to the strain energy release rate G (introduced in the previous section) by:

$$G = \frac{K^2}{E'} \tag{2.1.9}$$

where E' is the effective modulus of elasticity:

$$E' = \begin{cases} E & \text{(plane stress)} \\ \frac{E}{1-\nu^2} & \text{(plane strain)} \end{cases} \tag{2.1.10}$$

Fracture occurs when K reaches a critical value known as the **fracture toughness** K_{IC}, which is an intrinsic property of the material in plane-strain conditions:

$$K_{IC} = \sqrt{EG_c} \tag{2.1.11}$$

where G_c is the critical energy release rate from Griffith's theory [23].

2.2 Factors Affecting Fracture Toughness

The intrinsic properties of a material, such as microstructure and chemical composition, play a crucial role in determining fracture toughness. Key parameters include:

Effect of Grain Size

Grain size has a direct impact on fracture toughness. According to the **Hall-Petch relationship**, smaller grains increase yield strength, which in turn affects crack propagation resistance [29]:

$$\sigma_y = \sigma_0 + kd^{-1/2} \tag{2.2.1}$$

where:

- σ_y is the yield strength,
- σ_0 is a material constant,
- k is the Hall-Petch coefficient,
- d is the average grain diameter.

Since fracture toughness is related to plastic deformation at the crack tip, an increase in yield strength generally leads to a **decrease in K_{IC}** for brittle materials.

Second-Phase Particles and Inclusions

The presence of second-phase particles can either improve or degrade fracture toughness:

- **Fine precipitates (e.g., in Al alloys)** → Act as obstacles to dislocation motion, improving toughness.
- **Brittle inclusions (e.g., sulfides in steels)** → Act as crack initiation sites, reducing K_{IC}.

The **critical stress for crack initiation** due to inclusions can be approximated as [3]:

$$\sigma_c = \sqrt{\frac{2\gamma_s E}{\pi a}} \tag{2.2.2}$$

where:

- γ_s is the surface energy,
- E is the elastic modulus,
- a is the inclusion size.

Effect of Heat Treatment

Heat treatment affects the dislocation structure, residual stresses, and phase transformations, influencing K_{IC}:

- **Tempered martensite** → Higher fracture toughness than untempered martensite.
- **Aging in aluminum alloys** → Precipitate hardening increases strength but may reduce toughness.

2.2.1 Effect of Strain Hardening

Strain hardening, also known as work hardening, describes the phenomenon by which a ductile metal becomes progressively stronger and more resistant to further deformation after surpassing its yield point. As plastic strain accumulates, the density of dislocations within the material increases. These dislocations interact and hinder one another's movement, which makes subsequent plastic deformation more difficult. This mechanism effectively delays the nucleation, growth, and coalescence of voids, thereby enhancing the material's ductility and resistance to fracture.

Mathematically, the flow stress σ of a material undergoing strain hardening can often be expressed as a function of plastic strain ε_p using the Hollomon equation:

$$\sigma = K\varepsilon_p^n$$

where K is the strength coefficient and n is the strain hardening exponent. The value of n typically ranges between 0 (no hardening) and 1 (ideal hardening), and provides insight into the material's capacity to sustain uniform plastic deformation [30, 31].

Strain hardening increases the load-carrying capacity and delays the onset of localized deformation. This is evident in the evolution of the true stress–strain curve, which continues to rise after yielding. The tangent modulus, defined as $E_t = d\sigma/d\varepsilon$, gradually decreases but remains positive until necking occurs, indicating stable hardening behavior.

Stress triaxiality

Stress triaxiality η is typically defined as the ratio of the hydrostatic stress σ_m to the equivalent von Mises stress σ_{eq} [32]:

$$\eta = \frac{\sigma_m}{\sigma_{eq}} = \frac{1}{3}\frac{\sigma_1 + \sigma_2 + \sigma_3}{\sqrt{\frac{1}{2}\left[(\sigma_1 - \sigma_2)^2 + (\sigma_2 - \sigma_3)^2 + (\sigma_3 - \sigma_1)^2\right]}}$$

Elevated stress triaxiality promotes void growth and reduces the material's ability to undergo uniform plastic deformation, ultimately lowering its fracture toughness. As voids grow and link under high triaxiality, ductile fracture becomes more imminent [33].

To optimize a material's structural performance, especially in applications where ductile failure is a critical concern, it is essential to balance the beneficial effects of strain hardening against the detrimental influence of triaxial stresses. The critical void volume fraction and strain to fracture are strongly influenced by the interplay between strain hardening and the stress state.

Once the material reaches its ultimate tensile strength, it enters a phase of plastic instability, known as diffuse necking. During this stage, deformation begins to localize in certain regions of the specimen. This phenomenon is governed by the Considère criterion, which states that necking initiates when:

$$\frac{d\sigma}{d\varepsilon} = \sigma$$

Beyond this point, strain localization accelerates, and the material is no longer capable of sustaining uniform deformation. As loading continues, this localization evolves into a narrow deformation band, often inclined relative to the tensile axis, leading to the onset of the final fracture. This marks the transition to failure, characterized by a sharp drop in engineering stress as the material separates.

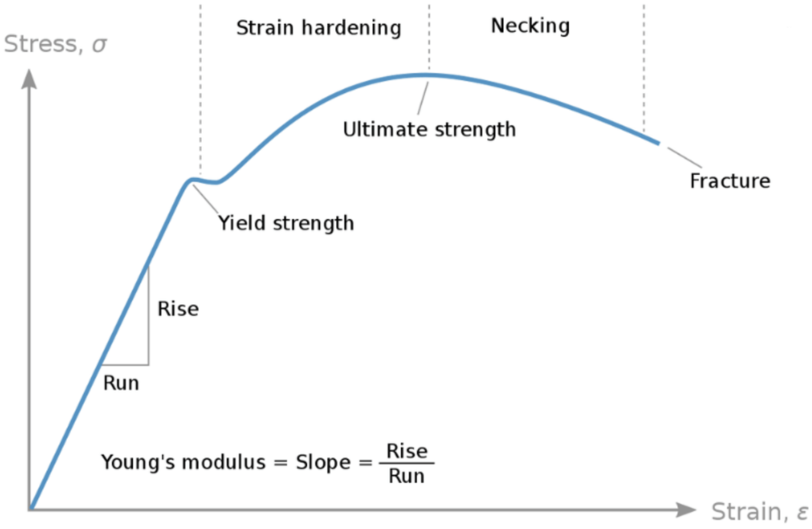

Figure 2.2.1: Stress-strain curve for a ductile material, highlighting strain hardening and necking [4]

2.2.2 Influence of Thickness

The thickness of a metallic sheet plays a crucial role in determining its fracture behavior, particularly in relation to the stress state that develops around flaws or cracks. As specimen thickness varies, the dominant stress state transitions between two fundamental regimes: plane stress and plane strain.

In thin sheets, the absence of significant out-of-plane constraints favors a plane stress condition, where stresses perpendicular to the specimen surface are negligible. This promotes extensive plastic deformation near the crack tip and a more distributed damage process, often resulting in higher apparent fracture toughness. Conversely, in thicker specimens, out-of-plane constraints inhibit deformation in the thickness direction, establishing a plane strain condition. This leads to a more confined plastic zone, elevated stress triaxiality, and a stronger tendency for void growth and coalescence near the crack tip, ultimately reducing fracture toughness.

Interestingly, the fracture toughness does not decrease monotonically with increasing thickness. Starting from thin specimens, it often increases to a peak value before declining. This non-monotonic trend is attributed to the interplay between geometric constraints and plastic zone development. In very thin specimens, although plastic deformation is extensive, the lower constraint can lead to early onset of necking and premature fracture, reducing the energy absorption capacity. The highest fracture toughness is typically observed at intermediate thicknesses, where plasticity is sufficiently developed without being overly restricted by through-thickness constraints.

The size and shape of the fracture process zone, defined as the region surrounding the tip of the crack where the microvoids nucleate and grow, are strongly dependent on the thickness. In thin sheets, this zone is wider and more elongated, allowing for a more efficient distribution of the strain and dissipation of energy. In contrast, thick specimens exhibit a more compact process zone due to higher constraint and reduced plasticity, leading to lower energy absorption before failure.

The complex relationship between thickness, stress state, and fracture resistance underscores the importance of carefully considering specimen geometry in both experimental characterization and structural design. Figure 2.2.2 schematically illustrates the typical variation of fracture toughness with specimen thickness, highlighting the peak at intermediate dimensions and the asymptotic behavior toward the plane strain limit.

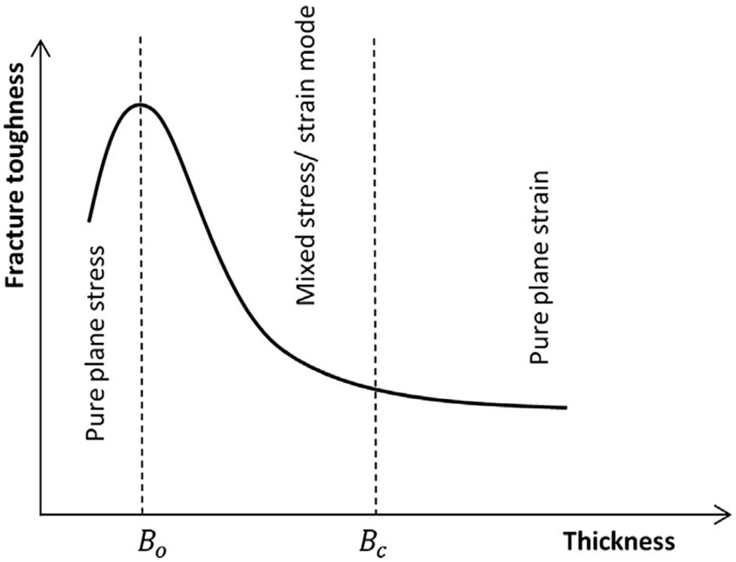

Figure 2.2.2: Dependence of fracture toughness on thickness of the specimen [5]

Understanding this thickness effect is essential when evaluating materials for structural applications where crack propagation resistance is critical. It also emphasizes the need for selecting representative specimen geometries in fracture testing to ensure meaningful and transferable material data.

2.3 Mechanisms of Fracture in Metallic Materials

2.3.1 Ductile vs. Brittle Fracture

Fracture behavior in metallic materials is typically classified into two main categories: *ductile fracture* and *brittle fracture*. These two mechanisms are distinguished by their deformation characteristics, energy absorption, and fracture surface morphology.

Ductile Fracture

Ductile fracture occurs when a material undergoes significant plastic deformation before failure. This type of fracture is usually characterized by the formation and coalescence of micro-voids. The process can be summarized in three main stages. Each of these stages is driven by the interaction between microstructural features and plastic deformation. The following summarizes this process.

1. **Nucleation of voids:**
    - Voids initiate primarily due to two mechanisms:

        (a) Decoherence at the interface between hard particles and the surrounding matrix.
        (b) Fracture of second-phase particles or inclusions within the matrix.
    - The probability of particle fracture increases with particle size, and is influenced by particle shape, orientation, and interfacial bond strength.
    - Nucleation typically occurs at stress concentrations, particularly in tensile stress states.

2. **Growth of voids:**
    - Void growth is driven by plastic deformation of the surrounding material, especially under high stress triaxiality.
    - Dislocations accumulate around the voids, promoting their expansion.
    - Voids formed from particle fracture tend to become spherical due to isotropic plastic deformation.
    - Voids resulting from particle-matrix separation are elongated in the direction of the applied load.

3. **Coalescence and final failure:**
    - Coalescence marks the transition from uniform deformation to highly localized plastic flow.
    - This occurs through:
        (a) *Internal necking*: load concentrates in the ligaments between voids, leading to localized thinning, similar to necking in tensile specimens.
        (b) *Shear coalescence*: plastic deformation is focused in microscopic shear bands, connecting voids through secondary microvoids.
    - In sheet metals, this transition alters the macroscopic fracture surface:
        - Fracture initiates at a notch or pre-crack with a flat, triangular region perpendicular to the load direction.
        - As damage progresses, the fracture surface tilts into a slant fracture, typically inclined at ∼ 45° relative to the loading axis.

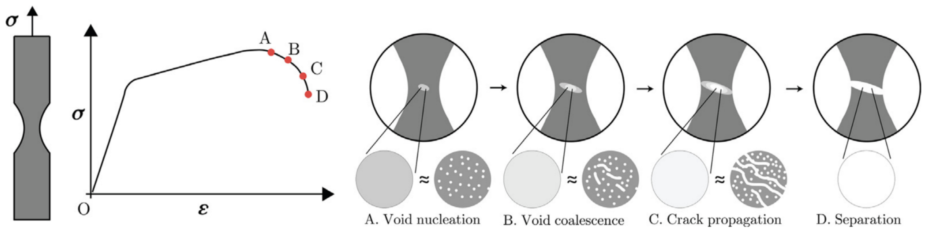

Figure 2.3.1: Micro-mechanical steps of ductile fracture [6].

Brittle Fracture

Brittle fracture, in contrast, occurs with little to no plastic deformation and is associated with rapid crack propagation. It is typically observed in materials with low toughness, such as high-strength steels or ceramics. The primary characteristics of brittle fracture include [34]:

- Sudden and catastrophic failure without significant prior deformation.
- Cleavage fracture, where crack propagation occurs along specific crystallographic planes.
- A relatively flat and faceted fracture surface, often featuring river patterns and chevron markings.

Brittle fracture is governed by the Griffith energy criterion, which states that a crack will propagate when the available elastic strain energy is sufficient to create new fracture surfaces:

$$G \geq G_c \tag{2.3.1}$$

where G is the strain energy release rate, and G_c is the critical strain energy release rate or fracture toughness [23].
The transition between ductile and brittle behavior depends on factors such as temperature, strain rate, and material microstructure.

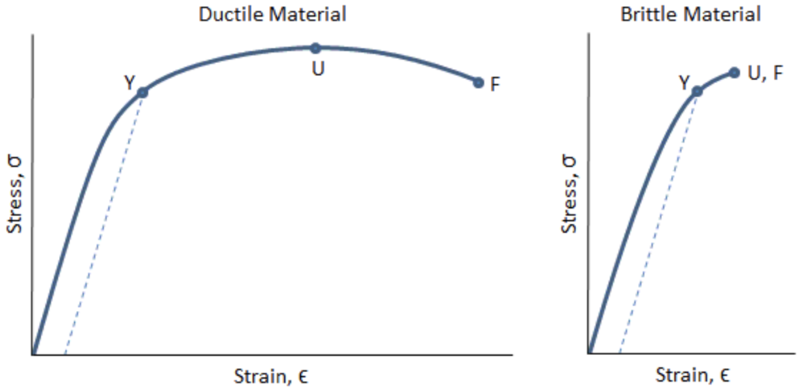

Figure 2.3.2: Stress-strain curves for a ductile material and a brittle material

2.4 Physics of ductile fracture

2.4.1 Crack Tip Plasticity and Small Scale Yielding (SSY)

The concept of *small-scale yielding* (SSY) is fundamental in linear elastic fracture mechanics (LEFM) and assumes that plastic deformation is confined to a region small relative to the overall dimensions of the structure and the crack length.

Plastic Zone at the Crack Tip

Under applied stress, the region near the crack tip experiences high stress concentration, leading to localized plasticity. The size of this plastic zone can be estimated using Irwin's approach [24], given by:

$$r_p = \frac{1}{2\pi} \left(\frac{K_I}{\sigma_Y} \right)^2 \tag{2.4.1}$$

where:

- r_p is the plastic zone radius.
- K_I is the mode I stress intensity factor.
- σ_Y is the yield strength of the material.

The presence of this plastic zone modifies the effective crack driving force and must be considered in fracture toughness assessments.

2.4.2 Elasto-Plastic Fracture Mechanics (EPFM)

While LEFM is valid for materials that exhibit minimal plastic deformation, many engineering materials undergo significant plasticity before fracture. Elasto-Plastic Fracture Mechanics (EPFM) extends fracture mechanics concepts to cases where plasticity is too large for LEFM to be applicable.

J-Integral

A fundamental concept in EPFM is the *J-integral*, introduced by Rice [35]. The J-integral represents a path-independent energy release rate and is defined as:

$$J = \int_\Gamma \left(W dy - T_i \frac{\partial u_i}{\partial x} ds \right) \tag{2.4.2}$$

where:

- W is the strain energy density.
- T_i are the traction components.
- u_i are the displacement components.
- ds is the arc length along the contour Γ.

For purely elastic materials, the J-integral reduces to the energy release rate G, making it a useful parameter for characterizing fracture even in elastic-plastic materials.

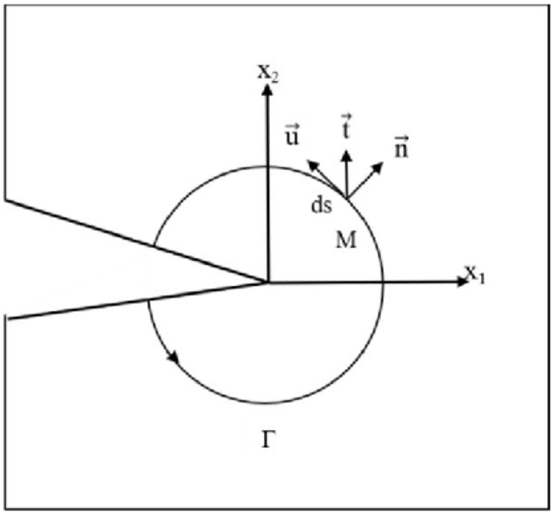

Figure 2.4.1: Definition of the J -integral contour [7]

2.4.3 Crack Tip Opening Displacement (CTOD)

Another key parameter in EPFM is the *Crack Tip Opening Displacement* (CTOD), which measures the separation between the crack faces near the tip. It is defined as [36]:

$$\delta = \frac{K_I^2}{E\sigma_Y} \tag{2.4.3}$$

where σ_Y is the yield strength. CTOD is particularly useful for assessing ductile fracture, as it provides a measure of the plastic deformation ahead of the crack tip.
An important parameter associated with the relationship between CTOD and the J-integral is the so-called *Shih factor*. This dimensionless coefficient, introduced by Shih [37], captures how the energy release rate correlates with the crack opening displacement, under the assumption of J-dominant fields. The relationship is expressed as:

$$\delta = \frac{d_n}{\sigma_0} J \tag{2.4.4}$$

where δ is the crack opening displacement, σ_0 is the yield stress, J is the J-integral, and d_n is the Shih factor, which depends on material hardening behavior and the geometry near the crack tip. The parameter d_n is typically derived for power-law hardening materials, taking into account the strain hardening exponent, initial strain, and other constitutive parameters.
The Shih factor essentially quantifies how constraints at the crack tip influence the distribution of plastic deformation. Under high constraint conditions, typical of plane strain, d_n tends to be lower, whereas under plane stress or reduced constraint, d_n increases. As a result, a higher J value is required to reach the same CTOD in high-constraint configurations. This reflects the shift in how energy is consumed, either elastically stored or dissipated plastically, in the vicinity of the crack front.

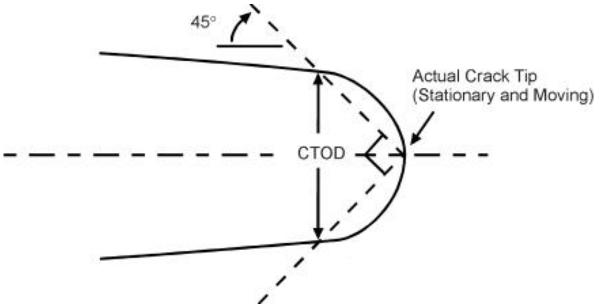

Figure 2.4.2: Determination of Crack Tip Opening Displacement (CTOD) [8]

Two key mechanisms play a fundamental role in influencing both the Crack Tip Opening Displacement (CTOD) and the stress distribution in the vicinity of a crack tip during ductile fracture. The first is crack tip blunting, as analyzed by McMeeking [38] within the framework of finite strain J2 plasticity. When a pre-cracked elastoplastic material is subjected to increasing tensile loading, the crack tip undergoes progressive blunting due to severe local deformation. Upon initiation of crack growth, the tip re-sharpens—a process often described as an unzipping mechanism occurring from one microstructural barrier to the next—resulting in a localized intensification of stresses just ahead of the crack front.

The second mechanism, known as crack tunneling, is observed during the through-thickness propagation of cracks in plate-like specimens. In this phenomenon, the central portion of the crack front tends to advance more rapidly than the regions near the free surfaces. This behavior is common in ductile fractures of metallic materials, such as steel and aluminum alloys. As shown by Lan et al. [39], this occurs because the middle section of the specimen typically experiences higher triaxial stress states, which promote earlier satisfaction of the fracture criterion. The elevated triaxiality in the interior enhances the nucleation, growth, and coalescence of voids, ultimately causing the crack to initiate and propagate preferentially at the mid-thickness before reaching the outer surfaces.

HRR Field and Large Scale Plasticity

For cases where plastic deformation is substantial, the stress and strain distributions near the crack tip are described by the Hutchinson-Rice-Rosengren (HRR) field [35, 40]. The stress distribution follows a power-law form:

$$\sigma_{ij} = \sigma_Y \left(\frac{J}{\sigma_Y l} \right)^{1/(n+1)} \tag{2.4.5}$$

where:

- l is a characteristic length.
- n is the strain-hardening exponent.

This model is crucial for describing crack growth in ductile materials.

EPFM provides a more accurate framework for analyzing fracture in engineering materials that do not conform to the assumptions of LEFM.

2.4.4 Essential Work of Fracture (EWF)

The *Essential Work of Fracture* (EWF) methodology [41] addresses thickness-dependent fracture toughness in **thin ductile plates** where conventional J-integral or CTOD approaches exhibit limitations. The EWF separates the total fracture work into two components:

- **Essential work** (w_e): Energy dissipated in the *fracture process zone* (FPZ) for material separation (void nucleation, growth, and coalescence).
- **Non-essential work** ($\beta w_p l_0$): Energy dissipated in the surrounding *diffuse plastic zone.*

For a Double Edge Notched Tension (DENT) specimen, the specific work of fracture w_f is expressed as:

$$w_f = \frac{W_f}{t_0 l_0} = w_e + \beta w_p l_0, \tag{2.4.6}$$

where W_f is the total work of fracture, t_0 is sheet thickness, l_0 is ligament length, and β is a plastic zone shape factor. The essential work w_e is obtained via linear regression of w_f versus l_0 for valid ligament lengths ($3t_0 \leq l_0 \leq W/3$).

Key insights from EWF:

1. *Thickness dependence*: w_e increases linearly with thickness t_0 due to enhanced crack-tip necking:

   $$w_e = \Gamma_0^{\text{plane stress}} + k t_0, \tag{2.4.7}$$

   where $\Gamma_0^{\text{plane stress}}$ is the **intrinsic plane stress toughness** (material separation work) and k quantifies necking dissipation.

2. *Intrinsic toughness*: $\Gamma_0^{\text{plane stress}}$ (e.g., 30 kJ/m^2 for aluminium 6082O) represents void-driven damage energy in the FPZ under low stress triaxiality, validated via micromechanical void-growth models.

3. *Advantages over J_i*: Unlike J-integral at initiation (J_i), w_e captures steady-state propagation resistance and avoids crack-advance measurement.

2.5 X-ray Computed Tomography

X-ray computed tomography (CT) is a non-destructive imaging technique that produces a three-dimensional representation of a specimen by combining multiple two-dimensional radiographic projections taken at different angles [42, 43]. It exploits the varying attenuation of X-rays within the material to reconstruct internal density differences, enabling visualization of features such as pores, cracks, inclusions and thickness variations [44]. In this study, X-ray tomography was specifically employed to measure crack length and size through the thickness of Al2050 specimens, providing critical three-dimensional validation of fracture behavior as detailed in Section 4.4.

2.5.1 Principles of X-ray Attenuation and Reconstruction

X-rays passing through a specimen are attenuated according to the Lambert–Beer law [42]:

$$I = I_0 \exp\big(-\mu\, x\big) \tag{2.5.1}$$

where I_0 is the incident intensity, I the transmitted intensity, μ the linear attenuation coefficient and x the path length [45]. By rotating the specimen and acquiring hundreds to thousands of radiographs, one obtains a set of projections $P_\theta(x')$. Reconstruction algorithms (e.g. filtered back-projection, algebraic reconstruction) then solve the inverse Radon transform to recover the spatial distribution of $\mu(x, y, z)$ [42, 43].
Micro-CT systems (Fig.2.5.1) achieve spatial resolution down to 0.5 μm using cone-beam geometry.

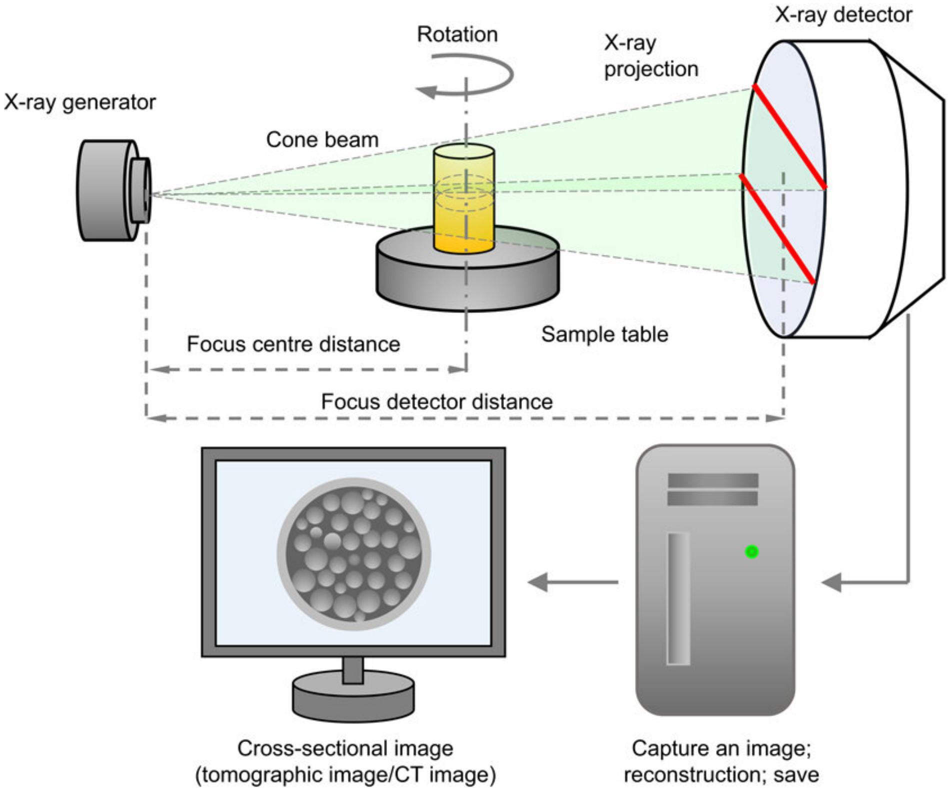

Figure 2.5.1: Schematic illustration of the working principle of micro CT [9]

2.5.2 Applications to Fracture Analysis of Al2050

X-ray computed tomography is particularly powerful in the study of ductile fracture, as it provides direct insight into internal damage mechanisms such as void nucleation, growth, and coalescence, processes that dominate failure in precipitation-hardened aluminum alloys such as Al2050 [44, 46].

In the context of this thesis, CT was used to examine the internal crack morphology of compact tension (DENT) samples made of Al2050-T8 with varying thicknesses (1 mm to 10 mm). The technique offers several key advantages over surface techniques such as SEM:

- **Three-dimensional void characterization**: The distribution, size and shape of microvoids can be measured volumetrically, revealing whether they are uniformly distributed or localized near the surfaces or mid-thickness regions. This is particularly relevant when comparing specimens in plane stress (thin) versus plane strain (thick) conditions.
- **Crack path and tunneling**: The evolution of the crack front along the thickness can be reconstructed, highlighting tunneling effects typically observed in thicker specimens due to triaxial constraint. In thinner specimens, cracks tend to remain more uniform across the section due to lower constraint.
- **Identification of fracture nucleation sites**: The initiation of cracks can often be linked to inclusions, second-phase particles, or pre-existing porosity. CT imaging enables the identification of such features even beneath the surface, offering insight into whether the fracture is particle-controlled or matrix-controlled.
- **Quantitative correlation with mechanical results**: By quantifying void volume fraction, crack opening profiles, and local damage fields, CT data can be correlated with CTOD (crack tip opening displacement) measurements, thus supporting or explaining observed trends in toughness as a function of thickness.

In addition, the non-destructive nature of CT allows for pre- and post-test scans of the same specimen, making it suitable for tracking damage evolution under load or after precracking steps. This complements the more localized and high-resolution information obtained from SEM fractography.

Overall, X-ray CT acts as a bridge between surface-based observations and bulk damage characterization, enriching the fracture mechanics analysis with volumetric insight that is essential when studying complex alloys and thickness-dependent behavior such as that exhibited by Al2050 [44, 46].

Chapter 3

Material Characterisation and Experimental Procedures

This chapter presents a comprehensive investigation of the mechanical and physical properties of the Al2050-T3 alloy, which was initially selected for subsequent crack opening displacement (CTOD) testing. The experimental work began with detailed material characterization - including microstructural analysis, chemical composition measurements, and mechanical testing - all carried out on T3 samples.

However, due to unforeseen delays and issues with the supply and preparation of Al2050-T3 samples, it was not possible to complete the full fracture toughness testing campaign on this alloy condition. As a result, all CTOD experiments presented in this thesis were instead performed on Al2050-T8 specimens. The switch to T8 was motivated by the need for consistent and timely testing, while maintaining compatibility in alloy system and manufacturing route.

Despite this change, the initial characterization of the T3 condition remains highly relevant for several reasons. First, it provides a well-defined reference for the base alloy's microstructure and properties. Second, it offers a basis for comparison with the T8 variant, helping to highlight the differences induced by the tempering treatment. These distinctions will be further discussed at the end of this chapter.

The experimental methodology begins with microstructural characterisation through metallographic preparation and chemical etching to reveal grain boundaries and phase distribution. The material's chemical composition is then quantitatively analyzed using Inductively Coupled Plasma (ICP) testing, complemented by Energy Dispersive X-ray Spectroscopy (EDX) for elemental mapping.

Mechanical behavior is evaluated through uniaxial tensile testing, while microhardness measurements are used to assess the homogeneity of the sample composition. Microstructural features are further examined using Scanning Electron Microscopy (SEM), with particular attention to the etched surfaces for phase identification and defect analysis.

Following complete material characterisation, the chapter details the CTOD testing protocol, including the essential pre-cracking procedure that precedes the main fracture toughness experiments. Special emphasis is placed on the surface preparation and etching requirements for accurate crack propagation monitoring during testing.

For the experimental investigation, the Al2050-T3 alloy was supplied by Constellium in the form of large-scale rolled plates with nominal dimensions of 2600 mm × 1400 mm × 60 mm (length × width × thickness). The as-received material underwent a systematic subdivision process to obtain specimens with appropriate geometries for the various characterization techniques and mechanical tests.

The plate was first sectioned using precision cutting equipment to produce smaller workpieces, which were then machined to final dimensions according to the specific requirements of each test configuration. Specimens were extracted along both the rolling direction (RD) and transverse direction (TD) to investigate potential anisotropy in mechanical properties. Particular attention was given to preserving the material's integrity during all cutting operations. The dimensional specifications and orientations of the prepared specimens will be detailed in the following sections, along with their respective applications in the experimental program.

3.1 Aluminum 2050 T3

The Aluminum 2050 T3 alloy, characterized by its "T3" temper, was the primary material investigated in this study. This temper indicates that the alloy has been subjected to a solution heat treatment, followed by cold working and natural aging. These processes enhance the alloy's mechanical properties, making it ideal for applications where a combination of strength and ductility is essential.
For this research, two Al2050 T3 plates were supplied by Costellium, one along the rolling direction (RD) and the other along the transverse direction (TD), to study potential anisotropy effects. The initial block dimensions were 260 mm × 140 mm × 60 mm (as shown in Figure 3.1.1), which were then machined to extract the specimens used for the analyses. The figure represents a portion of the technical drawings provided to the company for the procurement of the plates.

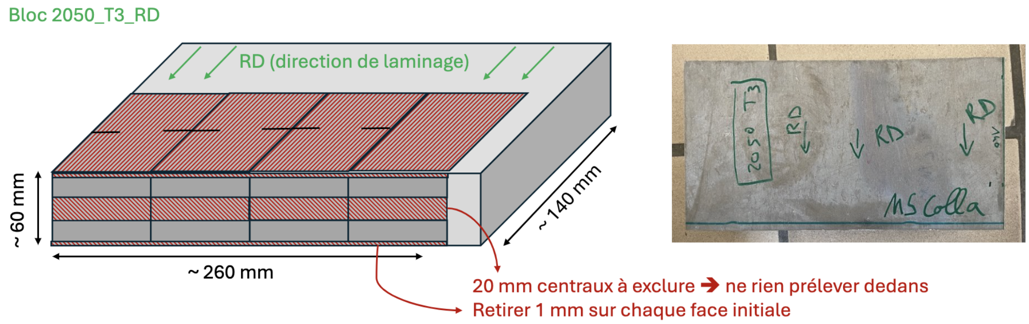

Figure 3.1.1: Part of the drawings provided to Constellium

3.1.1 Elemental composition of Al2050 T3

The elemental composition of the Al2050 T3 alloy was determined using Inductively Coupled Plasma (ICP) analysis, a technique that ionizes the sample in a high-temperature plasma to detect and quantify elements based on their emission spectra. The analysis, conducted by the LACaMi laboratory at UCLouvain, revealed the following weight percentages of the primary elements:
The ICP-OES results reveal that Al2050-T3 is a **aluminium-copper-lithium** alloy system, where aluminum naturally serves as the matrix element (94.2 wt.%). Copper constitutes the primary alloying addition (3.51 wt.%), consistent with its role in enhancing strength through precipitation hardening. Lithium appears as the third significant component (0.93 wt.%), crucial for density reduction and age-hardening capability.
Copper, the primary alloying element, is present in significant quantities, forming second-phase particles within the aluminum matrix. These particles, along with minor amounts of manganese and other elements, play a crucial role in influencing the material's mechanical behavior and fracture mechanisms.

3.1.2 Homogeneity through the thickness

To assess the material's homogeneity across its thickness, a microhardness testing was performed on two distinct Al2050 samples: one along the *rolling direction* (RD) and

Element	Weight %
Al (base)	94.20
Cu	3.51
Li	0.93
Mn	0.37
Mg	0.34
Ag	0.32
Zn	0.04
Ti	0.03
Fe	0.05
Si	0.01
Ga	<0.01
V	<0.01

Table 3.1.1: Elemental composition of Al2050 T3 (%wt) obtained by ICP analysis.

another along the *transverse to rolling direction* (TD). The tests covered the full 60 mm thickness of each sample using a standardized grid pattern of 120×3 indentations (360 measurement points total), with an approximate spacing of 0.5 mm between adjacent indentations to prevent overlap effects.

The tests were conducted using an Emcotest DuraScan G5 microhardness tester equipped with a Vickers diamond pyramid indenter, as illustrated in Figure 3.1.2. The microhardness testing was performed with a 0.2 HV load, corresponding to 200 grams applied.

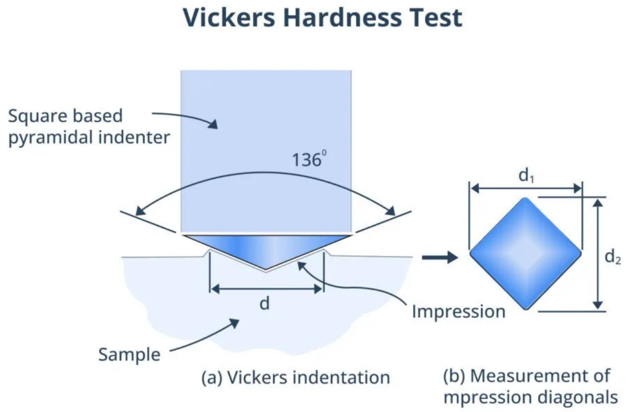

Figure 3.1.2: Schematic representation of the Vickers hardness test [10]

Prior to testing, all samples underwent meticulous mechanical polishing: the **surface preparation** involved sequential mechanical polishing using silicon carbide papers from P80 to P2400 grit. Each polishing step was performed for at least 5 minutes per level using the appropriate polishing machine to ensure uniform removal of material and surface quality.

The resulting hardness values predominantly ranged between 112 and 122 HV, showing good consistency throughout most of the material. However, the hardness mapping revealed localized variations in specific regions: between 10-20 mm from the surface in the rolling direction (RD) samples and in the central zone of the transverse direction

(TD) samples. This spatially confined variability suggests the presence of intermetallic particle clusters in these particular locations, rather than a uniform distribution across the entire central thickness. The correlation between these hardness fluctuations and the second-phase particle concentration will be quantitatively verified through a subsequent SEM analysis, which will provide both a morphological and a compositional characterization of the observed microstructural inhomogeneities.

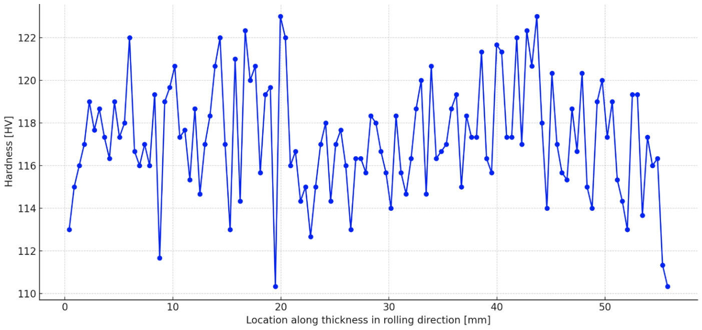

(a) Rolling direction (RD)

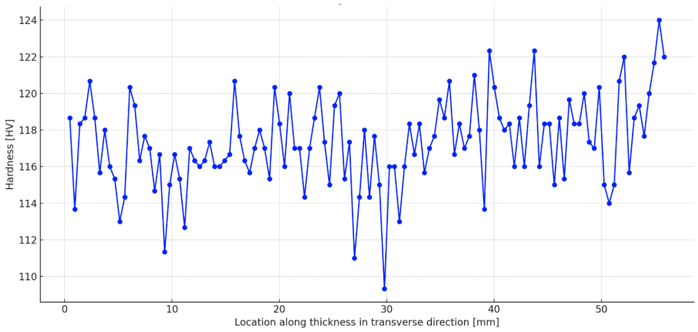

(b) Transverse direction (TD)

Figure 3.1.3: Microhardness profiles through thickness for (a) rolling direction and (b) transverse direction specimens

3.1.3 Chemical Etching of Al2050-T3 Alloy

To analyze the microstructure of the Al2050-T3 alloy, a chemical etching process was performed following standard metallographic procedures. Chemical etching is a widely adopted technique used to enhance the visibility of microstructural features such as grain boundaries, second-phase particles, and precipitates, which are not easily discernible on a mechanically polished surface. In particular, for aluminum alloys of the Al-Cu-Li family, Keller's reagent is commonly employed due to its effectiveness in selectively attacking the grain boundary regions, thereby enhancing contrast in optical microscopy.

The etchant was prepared using a modified version of the Keller's reagent. The composition is summarized in Table 3.1.2, which lists the volumes of each component used in the preparation of 200 ml of solution.

Component	**Volume [ml]**	**Concentration**
Distilled water	190	95%
Nitric acid (HNO_3)	5	2.5%
Hydrochloric acid (HCl)	3	1.5%
Hydrofluoric acid (HF)	2	1.0%

Table 3.1.2: Chemical composition of the Keller's reagent used for etching [12]

The preparation and application of the etchant were carried out under a fume hood with full personal protective equipment, including nitrile gloves, face shield, lab coat, and HF-specific safety materials, due to the highly corrosive and toxic nature of hydrofluoric acid.

The aluminum samples, previously polished to a mirror-like finish, were immersed in the etching solution for approximately 10 to 15 seconds. Immediately after, the samples were transferred into a separate beaker containing distilled water for about 20 seconds in order to quench the chemical reaction. This step was followed by a thorough rinse under running water and drying using compressed air and lint-free tissue. The etching process was repeated a second time to ensure a more uniform and well-contrasted surface finish. Upon completion of the procedure, all waste liquids were carefully collected and disposed of according to the laboratory's hazardous waste disposal protocols. The etched samples were then ready for microscopic analysis, with improved visibility of the microstructure facilitating further investigation of grain morphology, phase distribution, and possible surface defects.

3.1.4 Microstructural Observation and Results

Following the chemical etching procedure with Keller's reagent, the Al2050-T3 sample was examined under an optical microscope. At a magnification of 400x, the grain boundaries appeared clearly defined, indicating the effectiveness of the etching process in selectively revealing the microstructural features of the alloy. The contrast between the grain interiors and the boundaries was sufficient to enable a detailed qualitative analysis of the grain morphology and distribution.

The observed microstructure is consistent with what is typically reported in the literature for Al-Cu-Li alloys subjected to Keller's etching. According to previous studies

[47, 48], the presence of lithium in the alloy promotes grain refinement and facilitates the formation of well-defined grain boundaries when appropriately etched. Additionally, the use of hydrofluoric acid in the reagent enhances the selective attack of intergranular regions by dissolving the native oxide layer, allowing nitric acid to react more effectively with the underlying aluminum matrix.

This successful microstructural contrast is essential for subsequent evaluations, such as grain size measurements, deformation analysis, and the assessment of possible recrystallization or thermomechanical history. In this case, the uniformity and clarity of the etched surface confirm the suitability of both the reagent composition and the applied procedure.

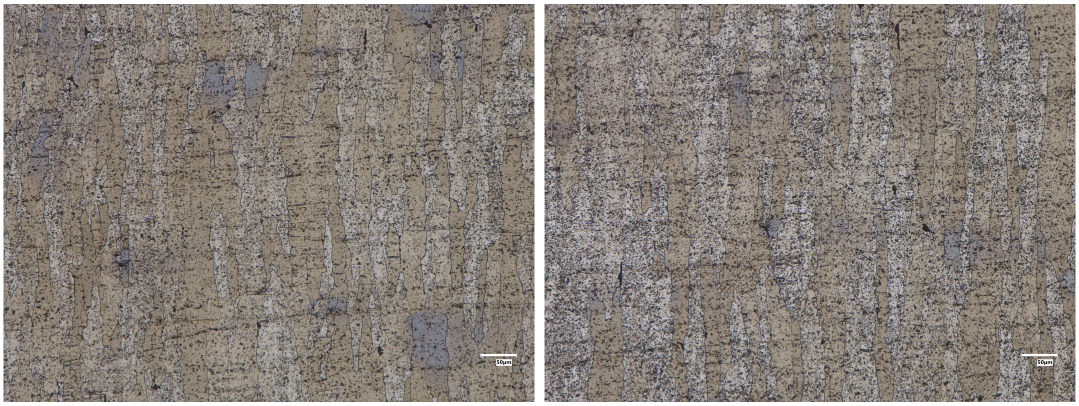

(a) Left edge (RD) (b) Center (RD)

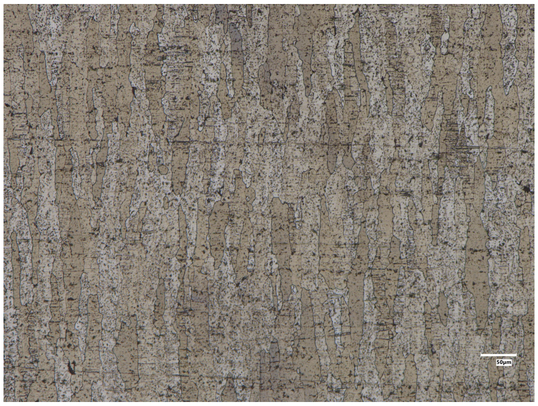

(c) Right edge (RD)

Figure 3.1.4: RD sample at 400× magnification showing grain structure after Keller's etching

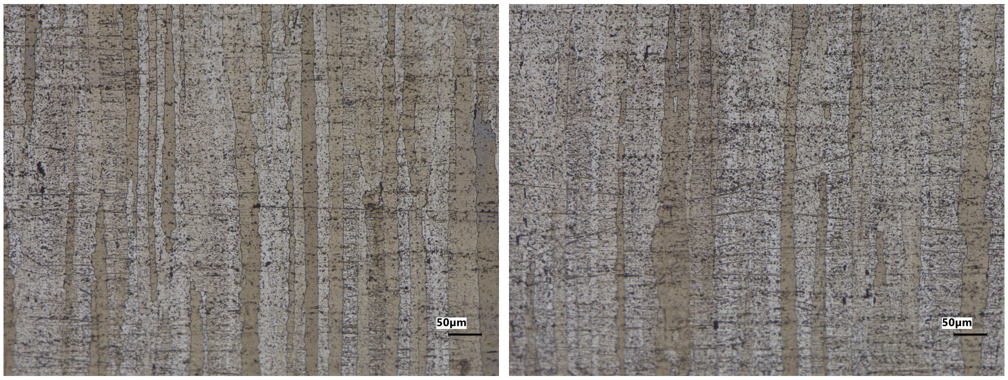

(a) Left edge (TD)

(b) Center (TD)

(c) Right edge (TD)

Figure 3.1.5: TD sample at 400× magnification showing grain structure after Keller's etching

To obtain higher resolution images and validate the optical microscopy observations, additional microstructural characterization was performed using a ZEISS Ultra 55 field emission scanning electron microscope (FE-SEM). The analysis was conducted at 300× magnification with an Extra High Tension (EHT) voltage of 15 kV, which provided optimal contrast and resolution for examining the grain structure while minimizing sample damage.
Three representative areas (1, 2 and 3 showed in Figure 3.1.6) were analyzed on both the RD (Rolling Direction) and TD (Transverse Direction) surfaces to ensure a comprehensive characterization of the sample. The SEM micrographs (Figures 3.1.7 and 3.1.8) revealed distinct differences in grain morphology between the two orientations. The RD surface exhibited elongated grains aligned parallel to the rolling direction, while the TD surface showed a more equiaxed grain structure, confirming the expected anisotropy resulting from the thermomechanical processing.

Figure 3.1.6: TD sample used for observations, highlighting the three areas: 1 left, 2 middle, 3 right

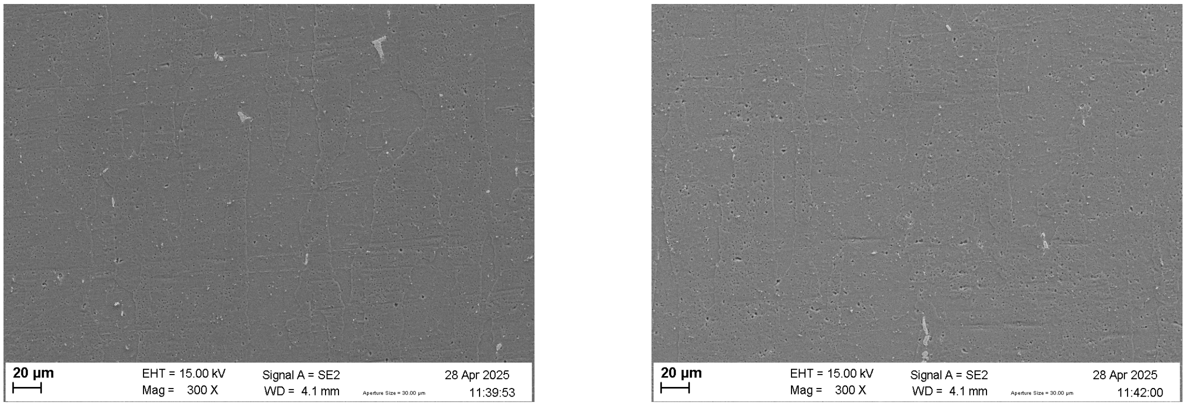

(a) Left section

(b) Middle section

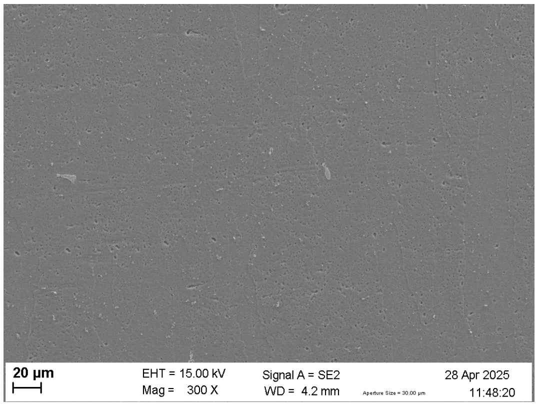

(c) Right section

Figure 3.1.7: SEM images through the thickness of the Al2050 plate (RD)

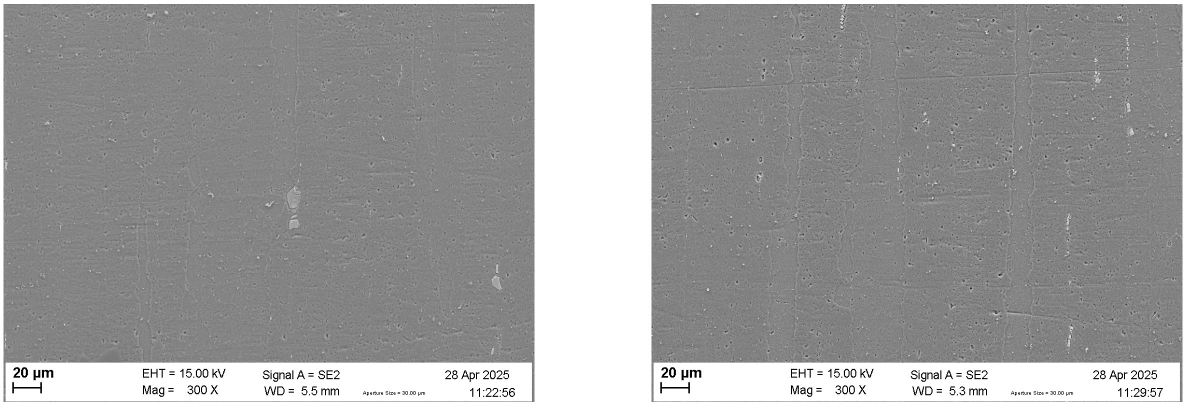

(a) Left section (b) Middle section

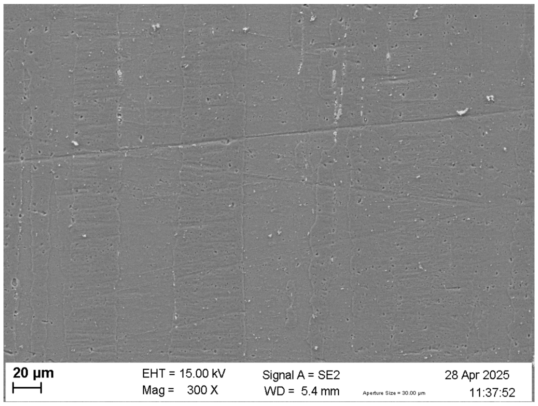

(c) Right section

Figure 3.1.8: SEM images through the thickness of the Al2050 plate (TD)

The resolution of the SEM enabled for a clear visualization of fine microstructural details, including secondary phase particles distributed along grain boundaries. These precipitates, likely consisting of Al-Cu or Al-Cu-Li intermetallic phases, were consistently observed across all examined sections, indicating homogeneous material processing. The 15 kV acceleration voltage proved particularly effective for this analysis, providing sufficient electron penetration to reveal subsurface features while maintaining good surface detail.

The combination of optical microscopy and SEM characterization at multiple sample locations provided a robust assessment of the microstructure of the material. The SEM analysis at 300× magnification complemented the optical microscopy results by offering higher resolution images. This multi-scale approach ensured comprehensive microstructural characterization of the Al2050-T3 alloy.

3.2 Crack Tip Opening Displacement (CTOD) Experiments on Al2050 T-8 Alloy

Before conducting experiments on Al2050-T3, tests were first performed on another aluminum alloy, **Al2050-T8**. While both tempers originate from the same base alloy, the T8 condition undergoes a significantly different processing route: after solution heat treatment, the material is cold worked and then subjected to artificial aging, unlike the T3 temper which relies on natural aging. This heat treatment sequence in T8 enhances strength through precipitation hardening but reduces ductility when compared to T3. Such differences are critical when evaluating fracture-related parameters, as they directly affect crack initiation and propagation behavior.

For the CTOD tests, Al2050-T8 specimens were machined from a single plate provided by Constellium, oriented along the rolling direction (RD). The decision to include T8 in the test campaign was motivated by the need to compare its fracture resistance with that of T3, especially under similar loading conditions. The mechanical response of T8 under quasi-static loading, in the presence of a fatigue pre-crack, is expected to reveal a different balance between strength and toughness, thereby offering a broader understanding of the alloy's performance envelope. The specimen geometry and testing procedures remained consistent across both tempers to ensure a reliable comparative framework.

3.2.1 Fatigue Pre-Cracking

The experimental investigation used double edge notched tension (DENT) specimens of aluminum alloy Al2050-T8. This specimen geometry was selected to ensure pure tensile loading conditions without compressive effects on the crack during propagation. Four distinct specimen thicknesses were examined: **1 mm**, **2 mm**, **4 mm**, and **10 mm**, with the detailed geometry illustrated in Figure 3.2.1. As an essential preparatory step, fatigue pre-cracking was performed to generate well-defined sharp cracks emanating from the machined notches. The pre-cracking parameters were carefully controlled to achieve crack extensions approximately three times greater than the original notch width, ensuring proper crack tip sharpness for subsequent CTOD testing.

The applied cyclic loading conditions (force amplitude and number of cycles) were optimized to produce controlled crack growth while avoiding excessive plastic deformation at the crack tip.

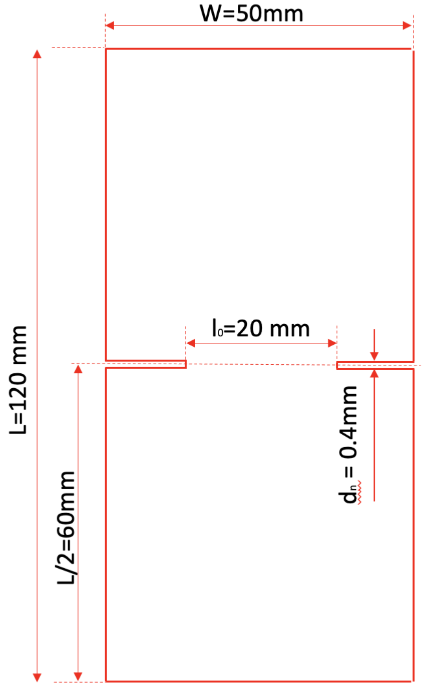

Figure 3.2.1: Geometry of the Al2050 T-3 specimen

The specific loading parameters for conducting fatigue pre-cracking on both thin and thick samples were adapted from a previous master's thesis on similar Al2050 specimens and testing conditions [49]. These values provided a practical starting point for defining the load ranges and cycle counts.
The exact number of cycles required to obtain a suitable pre-crack length was then determined through a trial-and-error process during preliminary tests. The initiation and growth of the pre-crack were carefully monitored every 2000 cycles using an optical microscope to ensure stable and consistent crack development across samples. The final parameters adopted for pre-cracking are reported in Table 3.2.1, which summarizes the average fatigue pre-crack conditions for samples with thicknesses of 1 mm, 2 mm, 4 mm, and 10 mm.

Thickness (mm)	**Cycles**	**Max Force (N)**	**Min Force (N)**	**Mean Force (N)**	**Frequency (Hz)**
1	10000	2000	200	1000	20
2	12000	2600	260	1300	30
4	10000	4200	420	2100	30
10	12000	14000	1400	7000	30

Table 3.2.1: Average fatigue pre-crack parameters of the samples

Following the fatigue pre-cracking, all samples were measured with a 3D microscope. Each parameter was measured on both sides of the notch for the five samples in each thickness group. The values in Table 3.2.2 show the average of these measurements (ten per thickness, combining the two sides of five samples). The ligament size after pre-cracking was calculated using the same averaging method.

Sample with thickness 1 mm	
Opening of notch	0.39 mm
Notch radius	0.19 mm
Pre-crack length	0.83 mm
Initial ligament distance	19.88 mm
Ligament size after precracking	18.22 mm

Sample with thickness 2 mm	
Opening of notch	0.38 mm
Notch radius	0.19 mm
Pre-crack length	1.58 mm
Initial ligament distance	20.01 mm
Ligament size after precracking	16.85 mm

Sample with thickness 4 mm	
Opening of notch	0.39 mm
Notch radius	0.18 mm
Pre-crack length	0.47 mm
Initial ligament distance	20.14 mm
Ligament size after precracking	19.22 mm

Sample with thickness 10 mm	
Opening of notch	0.38 mm
Notch radius	0.19 mm
Pre-crack length	0.80 mm
Initial ligament distance	19.90 mm
Ligament size after precracking	18.30 mm

Table 3.2.2: Averaged dimensions of the T-8 samples after fatigue pre-cracking

Following the 3D microscope measurements, representative images are presented below showing the crack characteristics for the 1 mm and 10 mm samples.

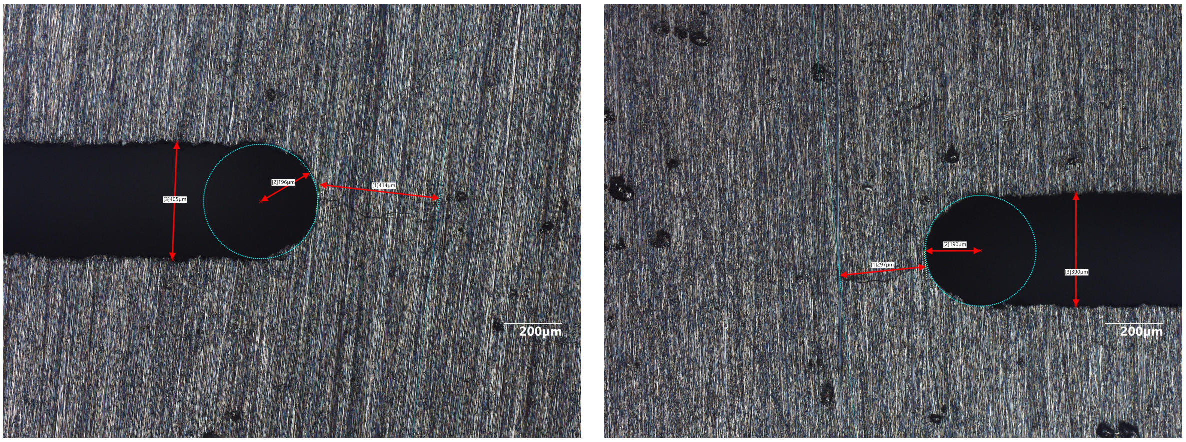

(a) Left crack measurement (b) Right crack measurement

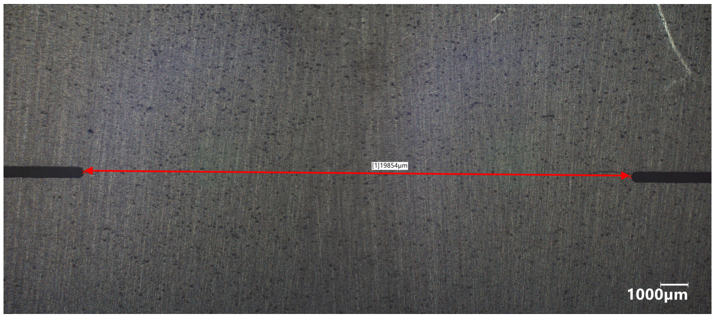

(c) Ligament distance measurement

Figure 3.2.2: 3D microscope images showing crack features for 1 mm thick sample

The images above clearly show the crack propagation characteristics in the 1 mm thick samples. Figures 3.2.2a and 3.2.2b demonstrate the left and right crack openings respectively, while Figure A.1.2c shows the initial ligament distance.

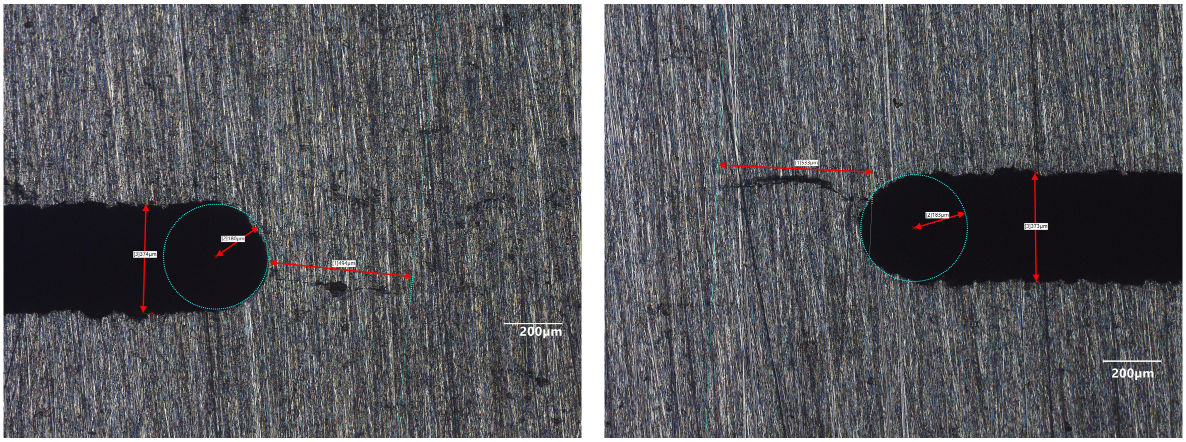

(a) Left crack measurement

(b) Right crack measurement

(c) Ligament distance measurement

Figure 3.2.3: 3D microscope images showing crack features for 10 mm thick sample

3.2.2 CTOD Testing Procedure

Traditional load-displacement curves often do not provide a clear indication of the precise moment at which fracture initiates in ductile metals. To overcome this limitation, the critical crack tip opening displacement (CTOD) has proven to be a reliable metric for estimating crack initiation. In this work, the indirect method proposed by Pardoen and Delannay [11] has been applied to determine the CTOD of two groups of aluminum alloy specimens, designed to represent plane stress and plane strain conditions by varying specimen thickness.

The approach is based on metallographic observation of the crack tip in unloaded specimens, which also enables insights into the underlying micromechanical damage mechanisms near the crack tip. Crack extension is understood to consist of two distinct phases: an initial stage of crack growth due to blunting and a subsequent stage corresponding to actual ductile tearing. The critical unloaded CTOD, denoted as δ_{CTOD}, is estimated as the difference between two key measurements: δ_1, the total opening of the blunted crack, and δ_2, the opening of the tearing crack at the same location, as illustrated schematically in Figure 3.2.4.

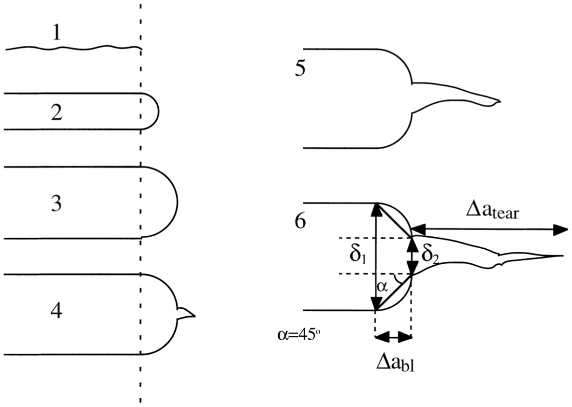

Figure 3.2.4: Schematic of crack tip evolution during CTOD test: δ_1, δ_2, and Δa [11].

For each group of specimens, three fatigue pre-cracked samples were subjected to tensile loading at a constant displacement rate of 0.5 mm/min, followed by unloading to produce a range of crack lengths. After testing, the specimens were cut, ground, and polished. A 3D optical microscope was then used to measure δ_1, δ_2, and the tearing extension $\Delta a_{\text{tearing}}$. Multiple grinding and polishing steps were performed to enable measurements along different thickness positions of each sample. This allowed the characterization of through-thickness averages for each parameter, accounting for the effect of crack tunneling—i.e., localized variations in crack extension due to constraint differences across the specimen thickness.
Once the experimental values of δ_1, δ_2, and $\Delta a_{\text{tearing}}$ were obtained, a plot of the difference $\delta_1 - \delta_2$ (representing the unloaded CTOD) versus $\Delta a_{\text{tearing}}$ was generated for each specimen group. By using multiple data points obtained from different crack lengths (at least three), a linear fit was applied to the plot. Extrapolating this fit allows one to estimate the unloaded CTOD at the point of crack initiation.

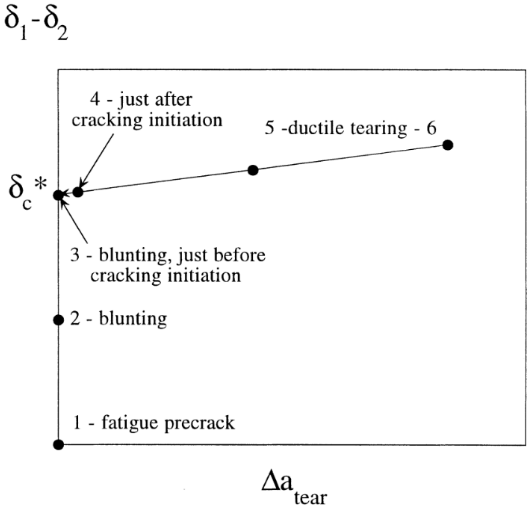

Figure 3.2.5: : Schematic of the plot used in multiple specimen method for determining the unloaded plastic CTOD [11].

3.3 Comparison between Al2050-T3 and Al2050-T8 Conditions

Although both T3 and T8 variants belong to the same Al-Cu-Li alloy system (Al2050), their processing routes result in significantly different mechanical and microstructural properties.

The T3 condition consists of solution heat treatment followed by cold working and natural aging, leading to a material with good ductility and moderate strength. In contrast, the T8 condition includes artificial aging after cold working, enhancing the precipitation hardening effect and increasing yield strength at the expense of ductility. These differences are expected to affect fracture resistance. In particular:

- **Ductility:** T3 is more ductile than T8, which typically allows for greater plastic deformation before crack propagation. This can lead to higher CTOD values under similar loading conditions.
- **Strength:** T8 offers higher tensile and yield strength, which may result in a sharper crack tip, reduced crack tip blunting, and therefore lower CTOD.
- **Fracture mode:** T3 is likely to exhibit more extensive crack tip plasticity and damage mechanisms associated with void coalescence, while T8 may be more prone to brittle fracture characteristics in high constraint conditions.

The T3 condition typically shows a yield strength between 350–400 MPa and ultimate tensile strength (UTS) in the range of 450–500 MPa, with elongation between 10–15%. The T8 temper, on the other hand, demonstrates higher strength (yield: 450–500 MPa; UTS: 500–550 MPa) but slightly lower ductility, with elongation values between 8–12%. Fracture toughness also differs between the two. The T8 condition generally exhibits 15–20% lower fracture toughness compared to T3, primarily due to increased brittleness caused by the dense precipitation of T1 phases. This is reflected in Crack Tip Opening Displacement (CTOD) measurements. CTOD is given by [14]:

$$CTOD = \frac{K_I^2}{m\sigma_y E} \tag{3.3.1}$$

where K_I is the stress intensity factor, σ_y the yield strength, E the Young's modulus, and m a constraint factor (typically 1.0–2.0 for aluminum alloys). Experimental tests show that T3 samples, such as T3-B1, tend to fail by ductile tearing with higher CTOD values, while T8 samples like T8-B2 often experience brittle fracture, demonstrating lower CTOD and crack growth resistance.

Microstructurally, T3 samples reveal elongated grains with sparse θ' precipitates, promoting plastic deformation and delaying crack initiation. Conversely, T8 samples exhibit a dense distribution of T1 precipitates, which increase strength but contribute to localized stress concentrations and early crack propagation [50].

These expected differences justify the separate discussion and motivate the analysis of T8 in the main experimental campaign, especially considering the need for consistent specimen preparation and reliable testing conditions.

Chapter 4

Experimental Results and Discussion

This chapter presents a comprehensive analysis of the mechanical characterization data, encompassing both tensile properties and Crack Tip Opening Displacement (CTOD) fracture toughness evaluations. The experimental methodology, detailed in Chapter 3, followed standardized protocols including ASTM E8 for tensile testing and ASTM E1290 for CTOD measurements.

Prior to quantitative assessment of the CTOD values, systematic fractographic examination was performed using scanning electron microscopy (SEM) to establish correlations between macroscopic fracture behavior and microscopic failure mechanisms. The integration of mechanical test data with fractographic evidence provides critical insights into the damage tolerance characteristics of Al2050-T3 alloy, particularly regarding the interaction between microstructure and crack propagation resistance. Quantitative results from these analyses are presented in Sections 4.1–4.3, with particular emphasis on the relationship between local strain hardening behavior and macroscopic fracture toughness.

4.1 Mechanical Testing results

The mechanical response of Al2050-T3 alloy was evaluated through uniaxial tensile testing of flat specimens with uniform 1 mm thickness, following ASTM E8 standards.

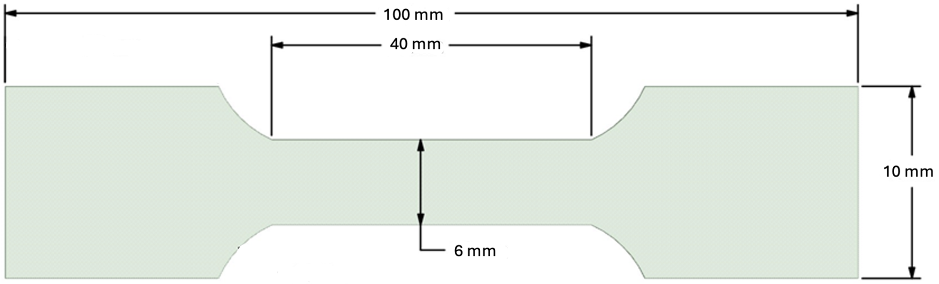

Figure 4.1.1: Geometry dimensions of the flat dog-bone tensile specimen (thickness: 1mm)

Four specimens were extracted from the rolled plate, two aligned with the rolling direction (RD) and two transverse to the rolling direction (TD) to assess potential anisotropy. Tests were conducted at a constant crosshead speed of 1 mm/min (equivalent to an initial strain rate of 3.33×10^{-4} s^{-1}), with strain measurements acquired via a 32 mm extensometer bonded to the gauge section.
The fundamental stress-strain relationships were established through:

$$\sigma_{eng} = \frac{F}{A_0}, \quad \epsilon_{eng} = \frac{\Delta L}{L_0} \tag{4.1.1}$$

where F is the applied load, A_0 the initial cross-sectional area (6 mm × 1 mm), and L_0 the original gauge length (32 mm). True stress-strain values were then derived from:

$$\sigma_{true} = \sigma_{eng}(1 + \epsilon_{eng}), \quad \epsilon_{true} = \ln(1 + \epsilon_{eng}) \tag{4.1.2}$$

The resulting true stress-strain curves were subsequently fitted with both Swift and Kocks-Mecking hardening laws, to extract material-specific hardening parameters.

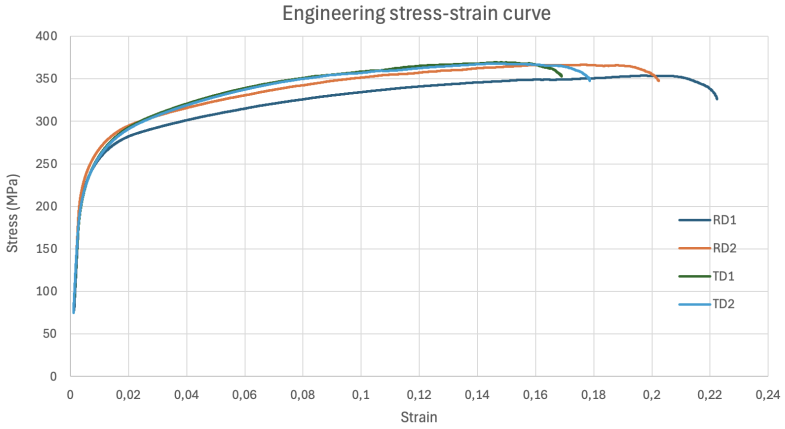

(a)

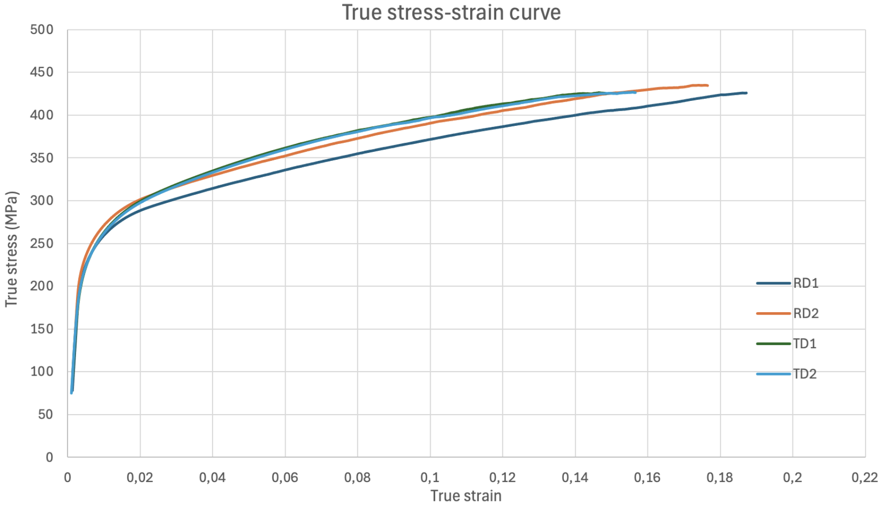

(b)

Figure 4.1.2: Engineering (a) and True (b) stress-strain curves for Al2050-T3 specimens tested in rolling direction (RD) and transverse direction (TD).

The following parameters were extracted from each stress-strain curve:
The **elastic modulus** (E) was determined as the slope of the initial linear region ($\epsilon < 0.2\%$) via linear regression, expressed as

$$E = \Delta\sigma/\Delta\epsilon|_{linear} \tag{4.1.3}$$

Yield strength values were calculated using the 0.2% offset method, where σ_y corresponds to the stress at the intersection between the stress-strain curve and a line parallel to the elastic modulus but offset by 0.002 strain, satisfying

$$\sigma_y = \sigma \quad \text{at} \quad \epsilon_{\text{offset}} = 0.002 + \frac{\sigma_y}{E} \tag{4.1.4}$$

The **ultimate tensile strength (UTS)** was identified as the maximum engineering stress prior to necking initiation.

$$\sigma_{\text{UTS}} = \max(\sigma_{\text{eng}}) \tag{4.1.5}$$

Fracture strain ϵ_f represented the engineering strain at specimen failure.

$$\epsilon_f = \epsilon_{\text{eng}}|_{\text{fracture}} \tag{4.1.6}$$

However, for a more accurate characterization of material ductility, particularly in the context of fracture mechanics, the true fracture strain (ϵ_{true_f}) provides better physical insight as it accounts for the instantaneous cross-section reduction during deformation. The true fracture strain was calculated using the logarithmic strain definition:

$$\epsilon_{\text{true}_f} = \ln(1 + \epsilon_f) \tag{4.1.7}$$

where ϵ_f is the engineering fracture strain from Equation 4.1.6. This transformation accounts for the nonlinear relationship between engineering and true strain during large deformations, particularly important after necking initiation.

Rolling Direction (RD)	
Elastic Modulus	67.87 GPa
Yield Strength	270.40 MPa
Ultimate Tensile Stress	364.69 MPa
True Fracture Strain	0.193

Transverse Direction (TD)	
Elastic Modulus	70.99 GPa
Yield Strength	254.68 MPa
Ultimate Tensile Stress	373.94 MPa
True Fracture Strain	0.160

Table 4.1.1: Averaged mechanical properties of Al2050-T3 in rolling direction (RD) and transverse to rolling direction (TD). The values represent the mean of two tested specimens for each orientation.

As presented in Table 4.1.1, a slight variation is observed in the mechanical properties of the Al2050-T3 alloy between the rolling direction (RD) and the transverse direction (TD). In particular, the elastic modulus and ultimate tensile stress are marginally higher in the transverse direction, while the yield strength and fracture strain show a modest reduction compared to the rolling direction.
These differences can be attributed to the anisotropic nature of rolled aluminum alloys, where the thermomechanical processing during rolling introduces a preferred grain orientation along the rolling direction. This grain alignment typically enhances ductility

and yield strength along RD while making the material slightly stiffer but more prone to earlier failure in the TD due to reduced capacity for plastic deformation.
Although the variation between RD and TD is not drastic, such anisotropy should be taken into account in the design of structures where directional mechanical properties can significantly affect performance, fatigue life, and failure modes under service conditions.

In addition to the standard mechanical properties, the material's hardening behavior was analyzed by fitting the true stress–true strain data to the **Swift strain hardening law**, defined as:

$$\sigma = A(\varepsilon_p + \varepsilon_0)^n \tag{4.1.8}$$

where σ is the true stress, ε_p is the plastic strain (obtained by subtracting the elastic portion from the true strain), A is the stress amplitude, ε_0 is a constant (typically small and non-zero to ensure numerical stability when $\varepsilon_p \to 0$), and n is the hardening exponent.
To determine A and n, the plastic region of the true stress–strain data was linearized by applying the natural logarithm to both sides of the equation, yielding:

$$\ln(\sigma) = \ln(A) + n \cdot \ln(\varepsilon_p + \varepsilon_0) \tag{4.1.9}$$

Then a linear regression was performed in Microsoft Excel using the transformed data, with $\ln(\varepsilon_p + \varepsilon_0)$ as the independent variable and $\ln(\sigma)$ as the dependent variable. The slope of the best-fit line corresponds to the hardening exponent n, and the intercept gives $\ln(A)$, from which A is obtained by exponentiation.

Direction	Rolling Direction (RD)	Transverse Direction (TD)
Stress Amplitude, A (MPa)	18.71	20.11
Hardening Exponent, n	0.345	0.392

Table 4.1.2: Averaged hardening law parameters for Al2050-T3

The results shown in Table 4.1.2 summarize the fitted parameters for the Swift strain hardening law. The transverse direction (TD) displays slightly higher values for both the stress amplitude A and the hardening exponent n, indicating a more pronounced strain hardening behavior compared to the rolling direction (RD). These differences can be attributed to anisotropic effects induced during the material's thermo-mechanical processing, which affect the material's plastic response depending on the loading orientation.

4.2 Fractographic Examination

Two Double-Edge Notched Tensile (DENT) specimens with distinct thicknesses (1 mm and 10 mm) were tested to fracture to characterize their mechanical response and fracture surfaces. This comparative analysis provides fundamental insights into thickness-dependent fracture behavior.

The experimental protocol included:

- Mechanical testing until complete fracture to record the force-displacement response
- Macroscopic fracture surface examination using 3D optical microscopy
- High-magnification analysis via Scanning Electron Microscopy (SEM)

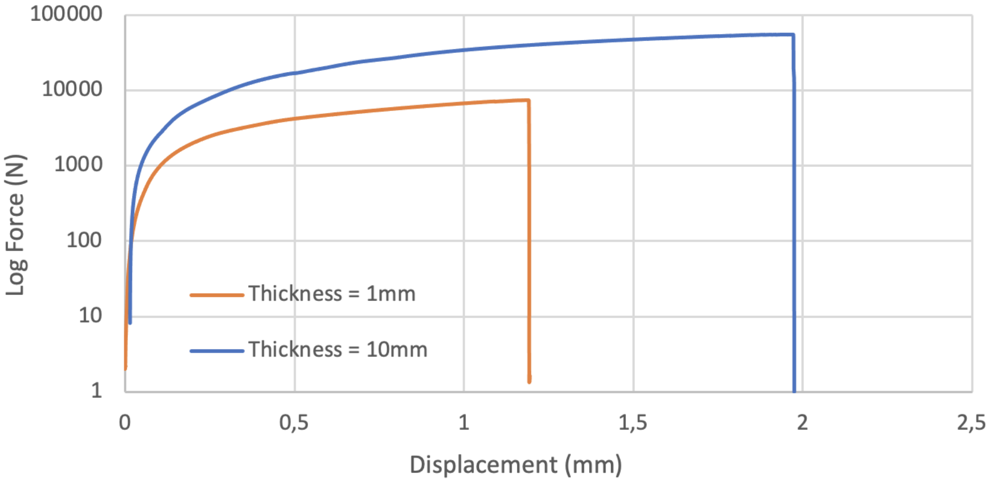

Figure 4.2.1: Logarithmic representation of force versus displacement for fractured DENT specimens with thickness of 1 mm and 10 mm

The maximum recorded values were:

Thickness	Max Displacement (mm)	Max Force (N)
1 mm	1.194	7,431.2
10 mm	1.975	55,213.8

Table 4.2.1: Maximum force and displacement values

The fracture surfaces exhibited distinct characteristics between the thin (1 mm) and thick (10 mm) specimens. The thinner specimen showed more pronounced plastic deformation features, while the thicker specimen demonstrated a more brittle fracture morphology with clearer crack propagation patterns.

1 mm sample

As clearly visible in the 3D microscopy image (Fig. 4.2.2), the fracture surfaces of DENT specimen revealed three distinct morphological zones, each corresponding to specific stages of crack propagation under tensile loading.

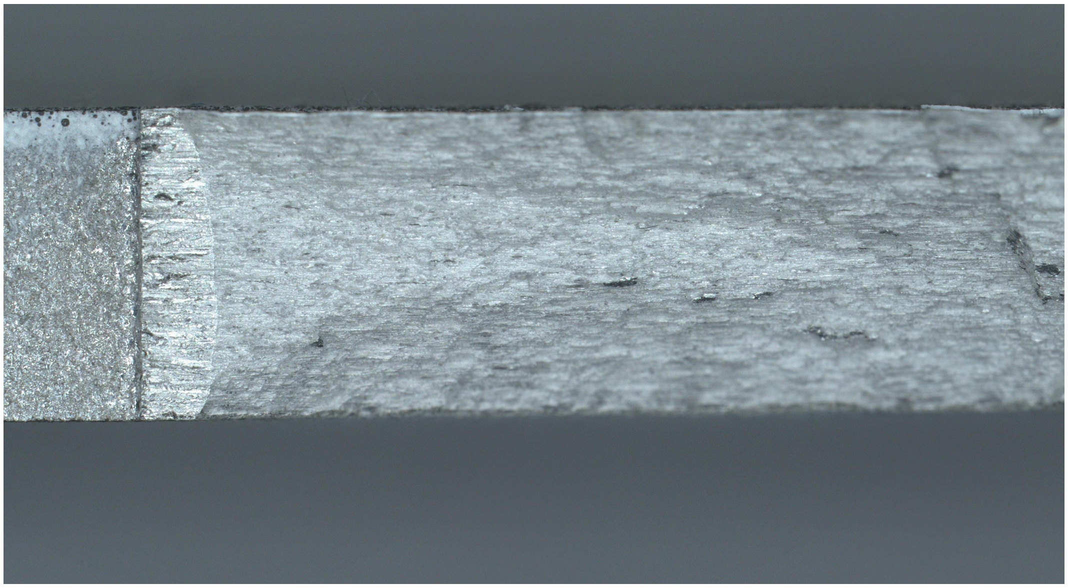

Figure 4.2.2: Fracture surface of the ligament area of 1mm thick sample

The fracture process initiates at the pre-cracked notch and evolves through three distinct phases:

1. **Fatigue Pre-Crack Zone**
   The fracture origin shows a smooth, featureless surface created during controlled pre-cracking. This region exhibits faint fatigue striations from cyclic loading and appears flatter than subsequent zones due to the slow, stable crack growth under compressive-tensile cycling. The pre-crack serves as a well-defined starting point for fracture analysis.

2. **Triangular Stable Growth Zone**
   Following initiation, the crack propagates perpendicular to the applied stress, forming a characteristic triangular pattern. This region displays typical ductile fracture morphology with dimpled surfaces, indicating void nucleation and coalescence. The increasing roughness from the apex to the base reflects the accelerating crack growth as stresses intensify.

3. **Slant Fracture Zone**
   The final failure occurs through shear deformation, creating 45° slant surfaces. These "shear lips" exhibit elongated dimples and striations aligned with the local shear direction. The extent of this zone depends strongly on specimen thickness, with thinner specimens showing more pronounced slant features due to dominant plane stress conditions.

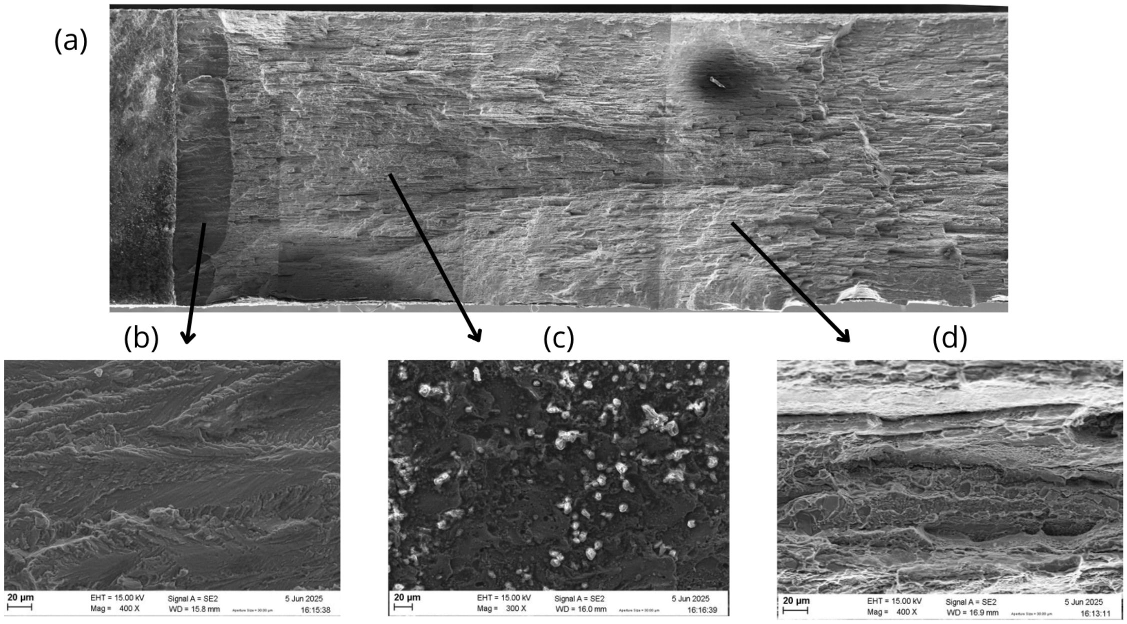

Figure 4.2.3: (a) SEM reconstructed image of the 1mm sample, (b) Fatigue Pre-Crack Zone, (c) Triangular Stable Growth Zone, (d) Slant Fracture Zone

The fracture morphology of the 1 mm specimen provides clear evidence of plane stress dominance throughout the failure process. Unlike thicker specimens that maintain a flat central fracture region, the complete development of slant fractures at approximately 45° across the entire specimen thickness indicates uniform through-thickness yielding. This consistent angular fracture surface, visible in both macroscopic examinations and SEM analysis, results from the material's ability to deform freely in the thickness direction under reduced constraint conditions.

The dimple morphology further confirms this stress state, with the slant zone exhibiting smaller, more uniformly sized dimples compared to thicker specimens - a characteristic feature of shear-dominated failure. Notably absent are the radial marks and large, irregular dimples typically associated with plane strain conditions, reinforcing the predominance of plane stress effects.

The observed tunneling phenomenon in the triangular transition zone offers particularly compelling evidence of the stress state transition. While the crack tip's central region maintains sufficient constraint to propagate perpendicular to the loading direction, the near-surface material yields to shear stresses, creating the characteristic "tunneling" profile where subsurface crack growth outpaces surface advancement. This behavior starkly contrasts with the fracture patterns observed in the 10 mm specimen, where greater through-thickness constraint maintains plane strain conditions over most of the crack front until final failure.

10 mm sample

The fracture surface morphology of the 10mm thick DENT sample reveals a more complex crack propagation behavior compared to the 1mm specimen, as illustrated in Figure 4.2.4. The 3D microscope image clearly shows three distinct regions: the initial wire-cut notch, a small fatigue pre-crack zone, and an extensive stable crack growth area. This latter region demonstrates a pronounced thickness-dependent behavior, with flat cracking dominating the central portion of the sample while slanted cracks develop near the free surfaces.

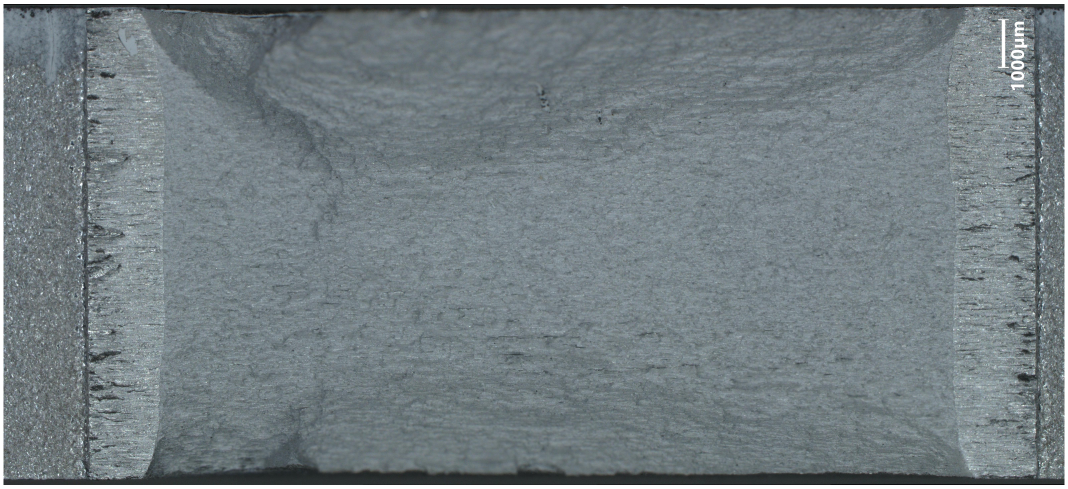

Figure 4.2.4: Fracture surface of the ligament area of 10mm thick sample

The transition in fracture morphology across the thickness direction is based on varying through thickness constraints. In the central region, the material's confinement creates conditions approaching plane strain, restricting deformation in the thickness direction and resulting in flat crack propagation. This flat fracture surface, visible in Figure 4.2.5, exhibits a dimpled morphology caused by intermetallics, similar to the triangular zone observed in thin samples but extending across the entire ligament area. Near the surfaces, where constraints diminish and conditions approach plane stress, the material deforms more freely, allowing the development of 45° slant cracks with characteristic elongated dimples and shear bands.

The fatigue pre-crack zone maintains a rough texture comparable to that observed in thin samples, suggesting similar initial crack growth mechanisms regardless of thickness. However, subsequent stable crack growth demonstrates fundamentally different behavior, with the thick sample maintaining a significant flat fracture region absent in thin specimens. This mixed-mode fracture surface, flat in the center and slanted at the surfaces, provides clear evidence of a transition from plane strain to plane stress conditions across the sample thickness, contrasting sharply with the uniform plane stress behavior observed in the 1mm specimen.

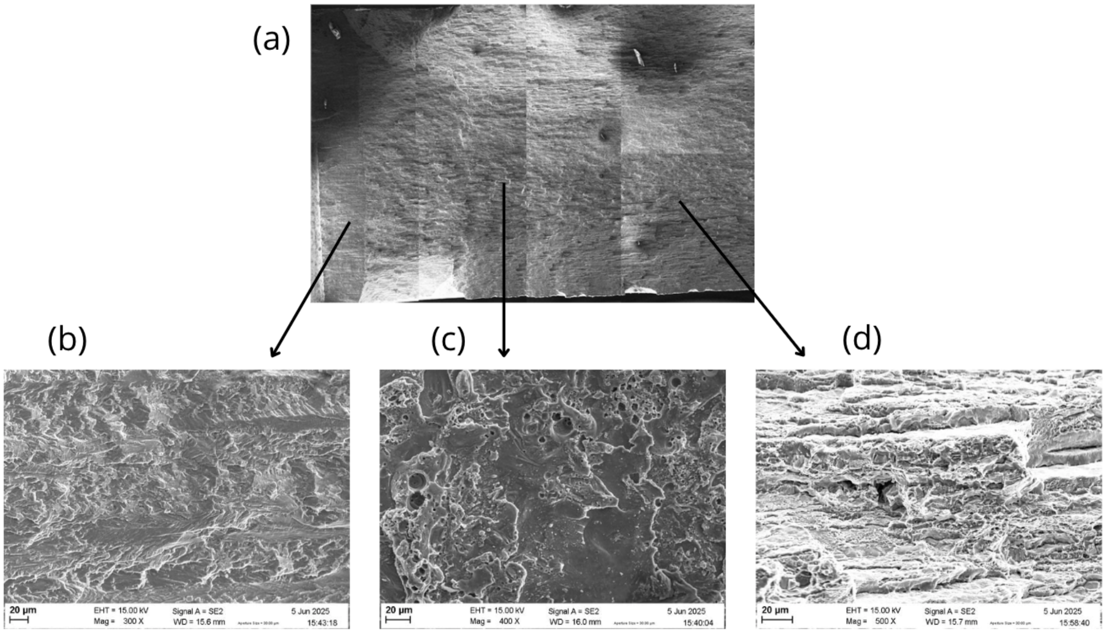

Figure 4.2.5: (a) SEM reconstructed image of the 10mm sample, (b) Fatigue Pre-Crack Zone, (c) Central flat crack region, (d) Surface slant crack zone

4.3 CTOD Test Results

The experimental program involved crack tip opening displacement (CTOD) testing of DENT specimens with four different thicknesses: 1 mm, 2 mm, 4 mm, and 10 mm. Due to variations in specimen preparation and occasional unintended fractures during pre-cracking or initial loading phases, the number of valid test specimens differed across thickness groups. All specimens were fatigue pre-cracked to ensure sharp crack tips prior to CTOD testing, as described in the subsection 3.2.1.

The maximum load and corresponding displacement for each specimen are summarized in the following Tables. These values represent the critical points where loading was reversed to prevent excessive crack growth while ensuring sufficient crack propagation for analysis.

1 mm Samples		
Sample	**Peak Load (N)**	**Peak Displacement (mm)**
Sample 1	7561,7	1,164
Sample 2	7840,2	1,216
Sample 3	7950,9	1,120
Sample 4	8273,7	1,168

Table 4.3.1: Peak load and displacement values for 1 mm thick samples

2 mm Samples		
Sample	**Peak Load (N)**	**Peak Displacement (mm)**
Sample 1	16021,7	1,987
Sample 2	14388,3	1,847
Sample 3	15711,6	1,976
Sample 4	15323,2	1,932

Table 4.3.2: Peak load and displacement values for 2 mm thick samples

4 mm Samples		
Sample	**Peak Load (N)**	**Peak Displacement (mm)**
Sample 1	18719,4	0,6553
Sample 4	20817,0	0,7448
Sample 5	30400,4	1,097

Table 4.3.3: Peak load and displacement values for 4 mm thick samples

10 mm Samples		
Sample	**Peak Load (N)**	**Peak Displacement (mm)**
Sample 1	52551,9	1,603
Sample 2	57150,1	1,784
Sample 3	58976,1	1,828
Sample 4	58573,0	1,913

Table 4.3.4: Peak load and displacement values for 10 mm thick samples

The peak load and displacement values for 4 mm thick specimens (Table 4.3.3) appear disproportionately low compared to other thicknesses. This deviation stems from experimental precautions taken during testing. Preliminary trials revealed that 4 mm specimens approached fracture at load levels just above those applied to 2 mm samples, yet significantly below the expected proportional scaling. To prevent premature failure that would compromise CTOD measurements, the loading protocol was conservatively limited to approximately 70% of the anticipated fracture load. This precautionary measure explains why Sample 5 (30,400 N) shows higher values than Samples 1 and 4; the latter were intentionally unloaded earlier in the test sequence to preserve crack tip integrity. The decision prioritized obtaining valid CTOD measurements over achieving complete force-displacement curves, as the primary research objective focused on crack initiation behavior rather than full fracture characterization. This experimental constraint particularly affected 4 mm specimens because their thickness places them near the critical transition zone between plane stress and plane strain dominance, where small load variations disproportionately influence crack stability.

The load-displacement curves obtained from CTOD testing are presented in Figures 4.3.1 through 4.3.4, showing the mechanical response of specimens with thicknesses of 1 mm, 2 mm, 4 mm, and 10 mm respectively.

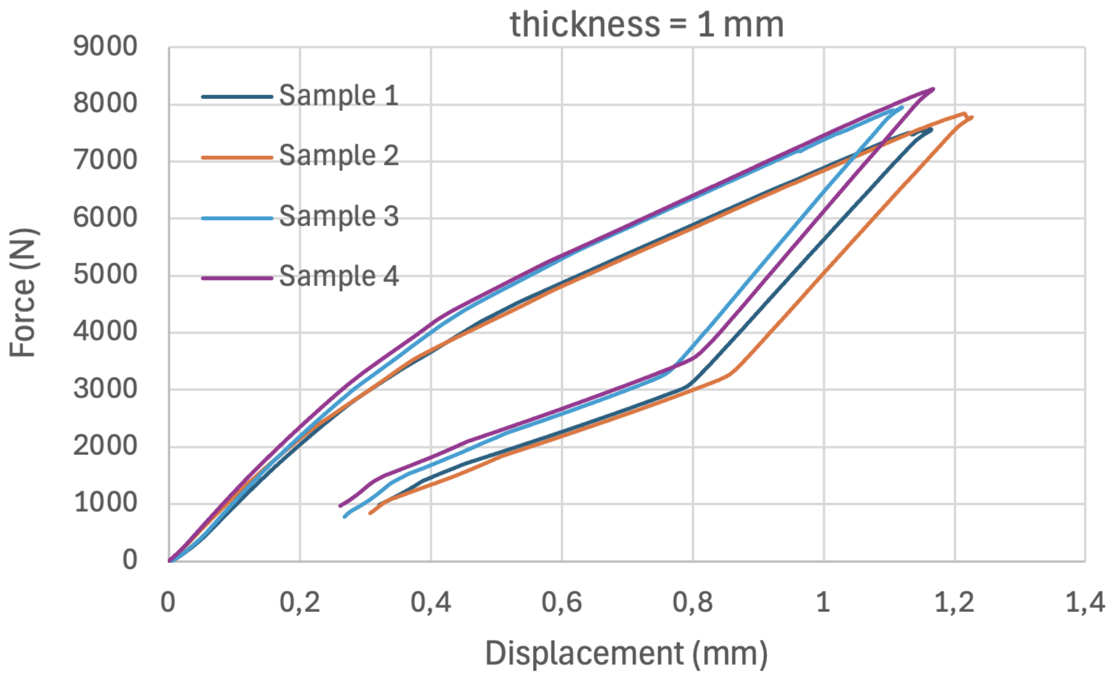

Figure 4.3.1: Load-displacement curves for 1 mm thick DENT specimens

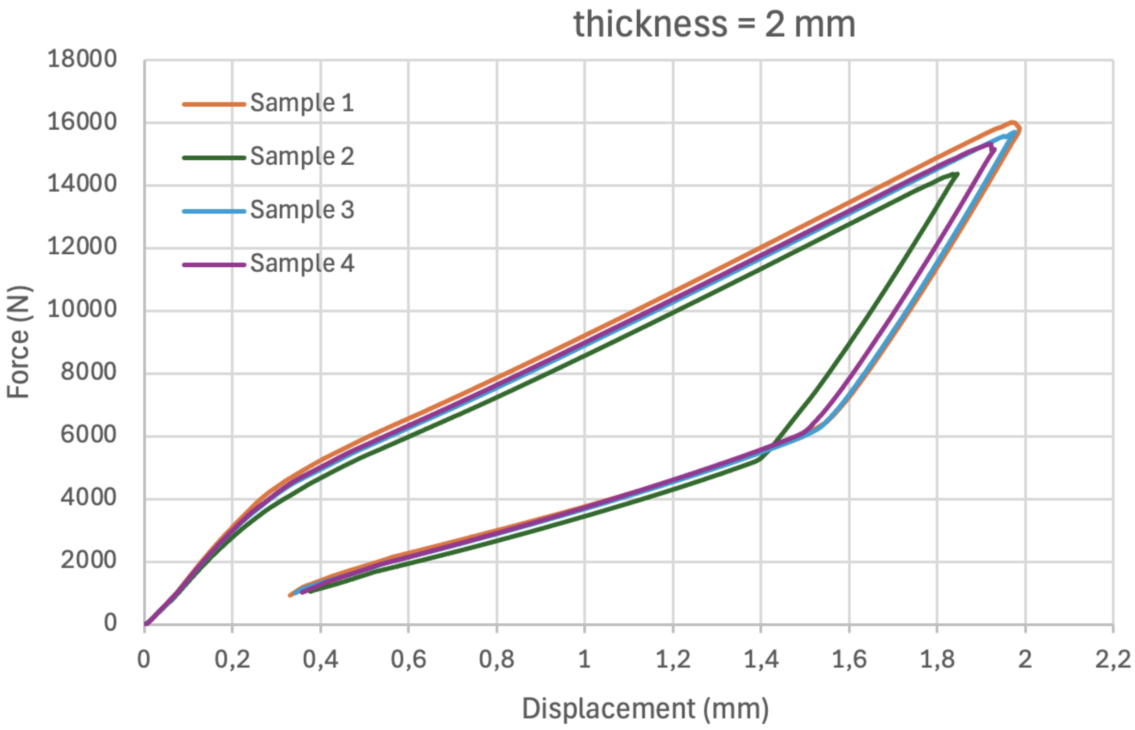

Figure 4.3.2: Load-displacement curves for 2 mm thick DENT specimens

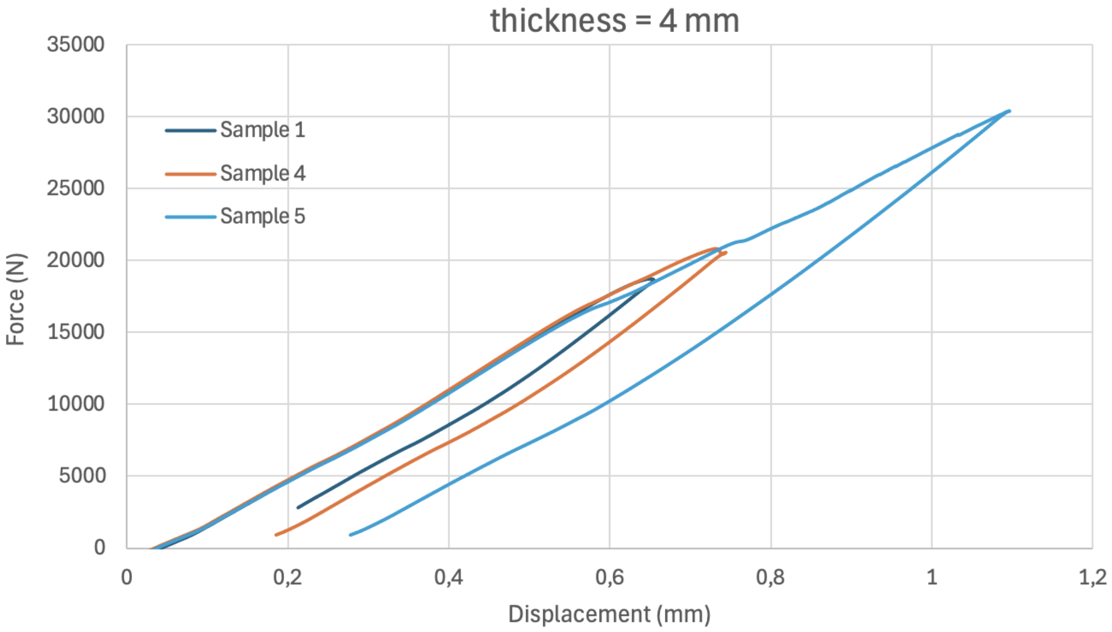

Figure 4.3.3: Load-displacement curves for 4 mm thick DENT specimens

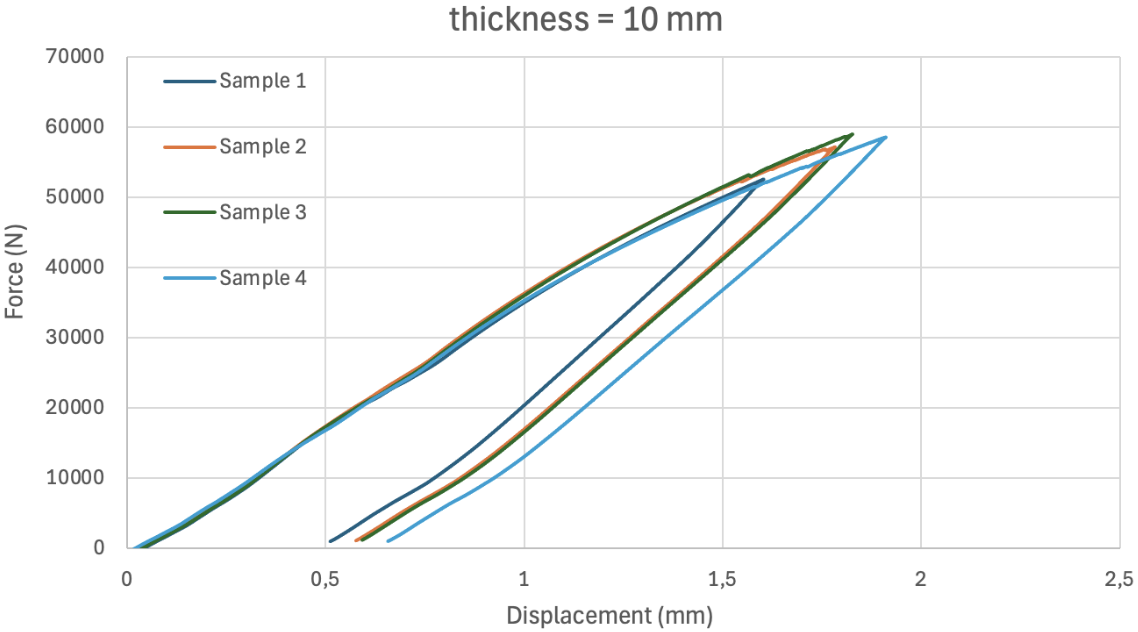

Figure 4.3.4: Load-displacement curves for 10 mm thick DENT specimens

The load-displacement curves exhibit distinct hysteresis behavior during unloading, particularly in thin specimens (1–2 mm), as visible in Figures 4.3.1 and 4.3.2. This phenomenon manifests as a non-linear recovery path during unloading, forming a closed loop with the loading curve. Three primary mechanisms contribute to this effect:

- **Plasticity-dominated recovery**: In thin specimens, the reduced constraint allows greater through-thickness plastic deformation at the crack tip. During unloading, reverse plasticity occurs asymmetrically due to Bauschinger effects, creating the hysteresis loop [51].
- **Plane stress dominance**: The 1–2 mm thickness range approaches full plane stress conditions, enabling larger crack-tip blunting and residual deformation. This contrasts with the near-plane-strain behavior of 10 mm specimens, where triaxial constraints suppress blunting and promote linear-elastic recovery.
- **Geometric instability**: Thin specimens are prone to out-of-plane buckling during unloading, which introduces additional energy dissipation not captured by conventional fracture mechanics models. Microstructural observations confirm this through asymmetric crack-face contact patterns.

The hysteresis magnitude correlates with thickness-dependent plasticity: thin specimens (1–2 mm) exhibit significantly larger energy dissipation (quantified in prior studies [26, 52] as ∼10–15% of total work), while thick specimens (10 mm) show minimal dissipation (<5%).

The tabulated data demonstrates consistent reproducibility across thickness groups, with the exception of the 4 mm specimens due to the modified loading protocol discussed previously. For the 1 mm, 2 mm, and 10 mm samples, the peak loads and corresponding displacements show minimal variation within each thickness group, reflecting stable crack initiation behavior and reliable experimental repeatability. This consistency suggests that material heterogeneity had negligible effects on the mechanical response for these thicknesses. The displacement at peak load proves particularly repeatable, further confirming the robustness of the testing methodology for specimens where full fracture progression was allowed.

4.4 X-ray Computed Tomography Results

As explained in Section 2.5, X-ray computed tomography provides unique capabilities for three-dimensional fracture characterization by reconstructing internal structures through differential X-ray attenuation. Applying these principles, we performed comprehensive analysis of crack propagation using the RX Solutions EasyTom S micro-CT system, which provided crucial insights into thickness-dependent fracture behavior. With an achieved voxel size of 4.8 μm the scans enabled high-resolution reconstruction of crack paths across all specimen thicknesses (1 mm, 2 mm, 4 mm, and 10 mm).
The tomographic data was processed using ImageJ software, where the known voxel size allowed precise measurement of crack dimensions at standardized intervals. This systematic approach leveraged the technique's capability for through-thickness analysis to quantify key fracture parameters.

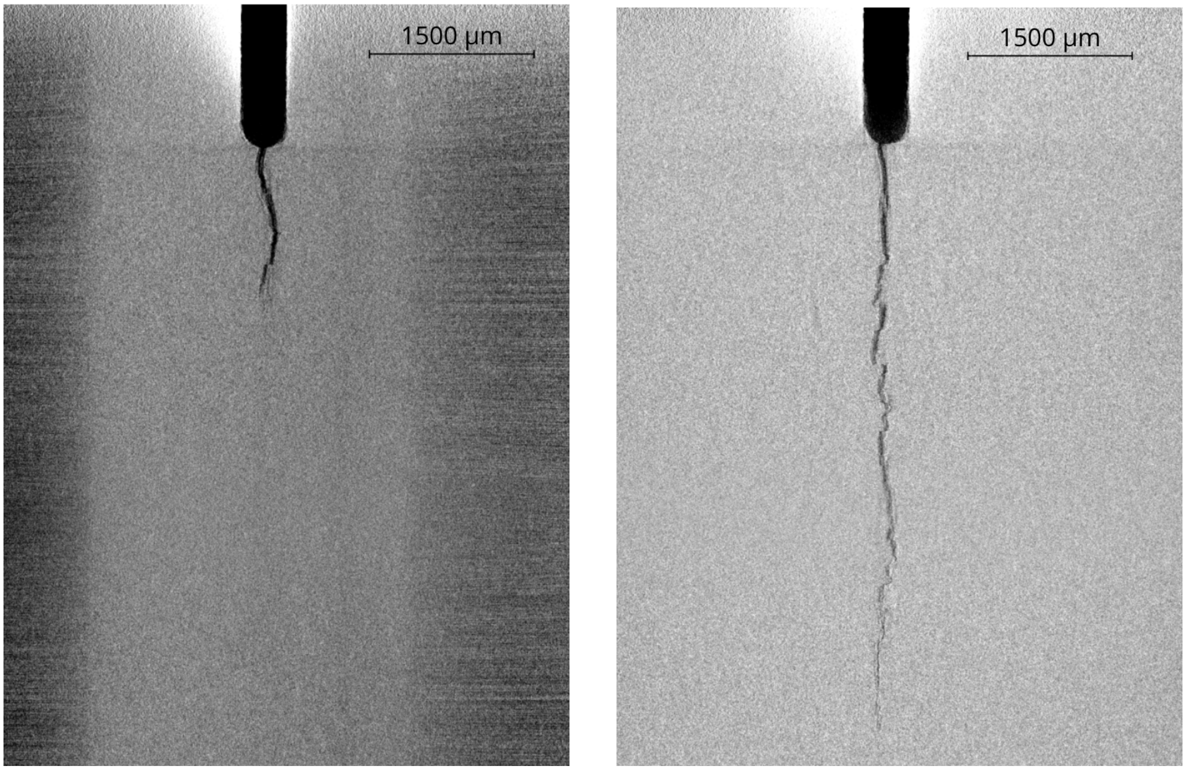

(a) Surface view showing crack initiation and initial propagation

(b) Mid-thickness view demonstrating advanced crack tunneling

Figure 4.4.1: Comparative X-ray tomography images of 10 mm thick specimen showing through-thickness crack progression differences

The comparative images in Figure 4.4.1 provide direct visual evidence of the tunneling phenomenon discussed in Section 2.5. While the surface view (Fig. 4.4.1a) shows relatively uniform crack propagation, the mid-thickness section (Fig. 4.4.1b) reveals significantly advanced crack growth, with the crack front curvature characteristic of plane strain conditions.
The distribution of crack extension, Δa, through the sample thickness is shown in the following Figures, separately for each notch of the DENT specimens.

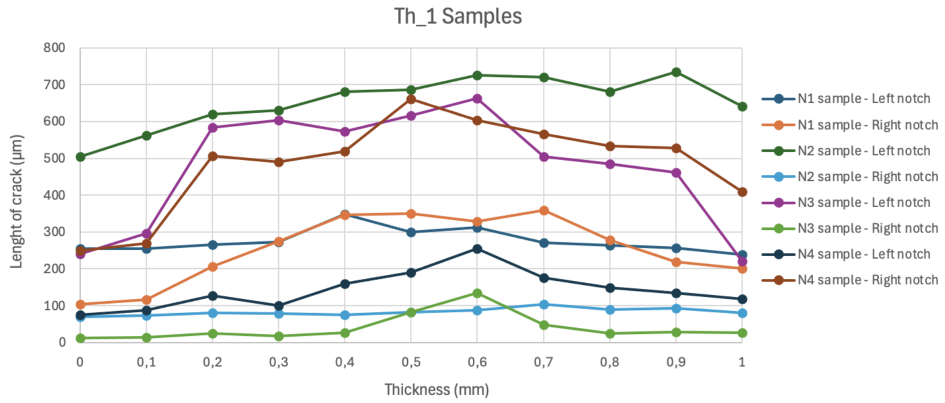

Figure 4.4.2: Δa through the thickness of samples with thickness of 1 mm

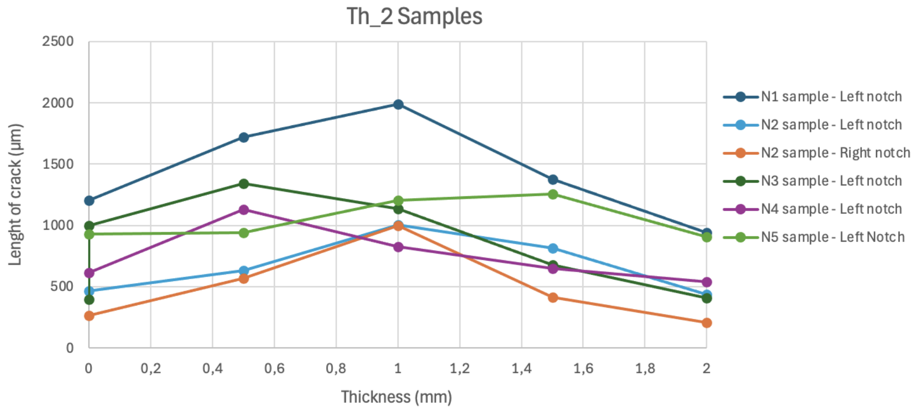

Figure 4.4.3: Δa through the thickness of samples with thickness of 2 mm

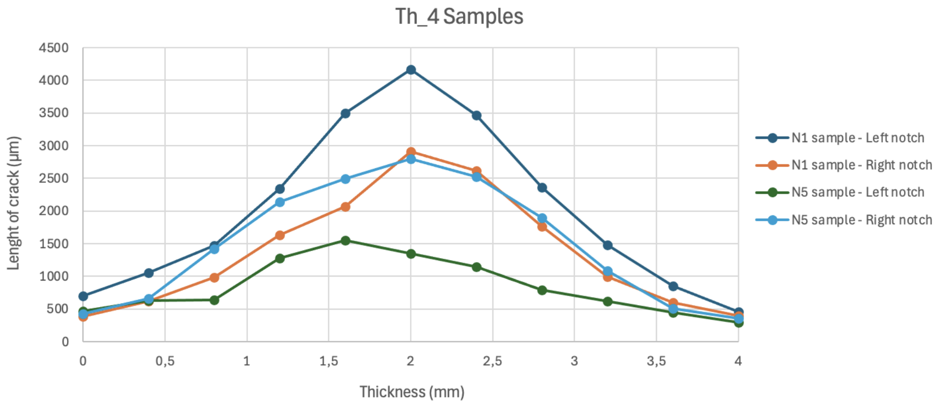

Figure 4.4.4: Δa through the thickness of samples with thickness of 4 mm

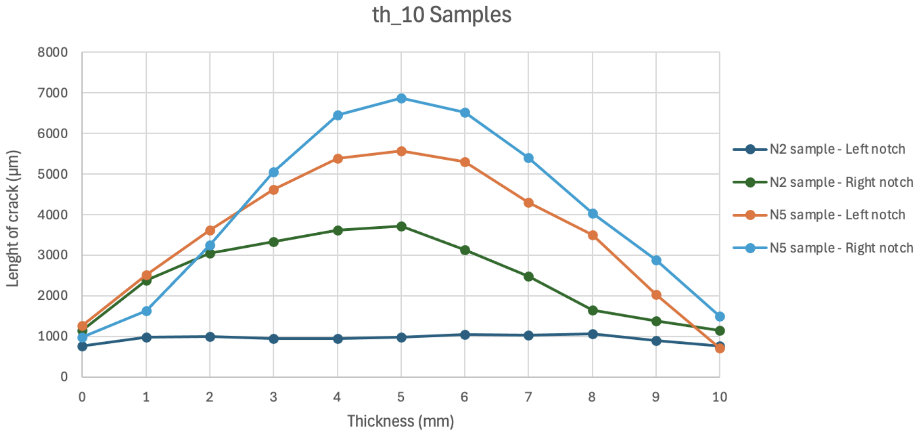

Figure 4.4.5: Δa through the thickness of samples with thickness of 10 mm

The results consistently show that the maximum Δa is located near the mid-thickness of the specimens, revealing a clear tunneling behavior that is not detectable through surface-level measurements. Minor discrepancies or overlapping trends in the Δa values between notches of the same specimen may stem from variations in pre-crack dimensions. These can be linked to slight misalignments during fatigue pre-cracking or small geometric differences in the EDM-machined notches.
In addition, measurements of the blunted crack opening, δ_1, and the tearing crack opening, δ_2, were performed along the thickness of each DENT sample for both notches. The difference between δ_1 and δ_2 was used to compute the Crack Tip Opening Displacement (CTOD), which was then plotted as a function of Δa in Figure 4.4.6. A linear fit was applied to the scattered data, and by extrapolating the line to the $\Delta a = 0$ intercept, the critical CTOD, δ_c, was obtained for each thickness. This critical value serves as an indicator of the fracture toughness for each group of specimens.

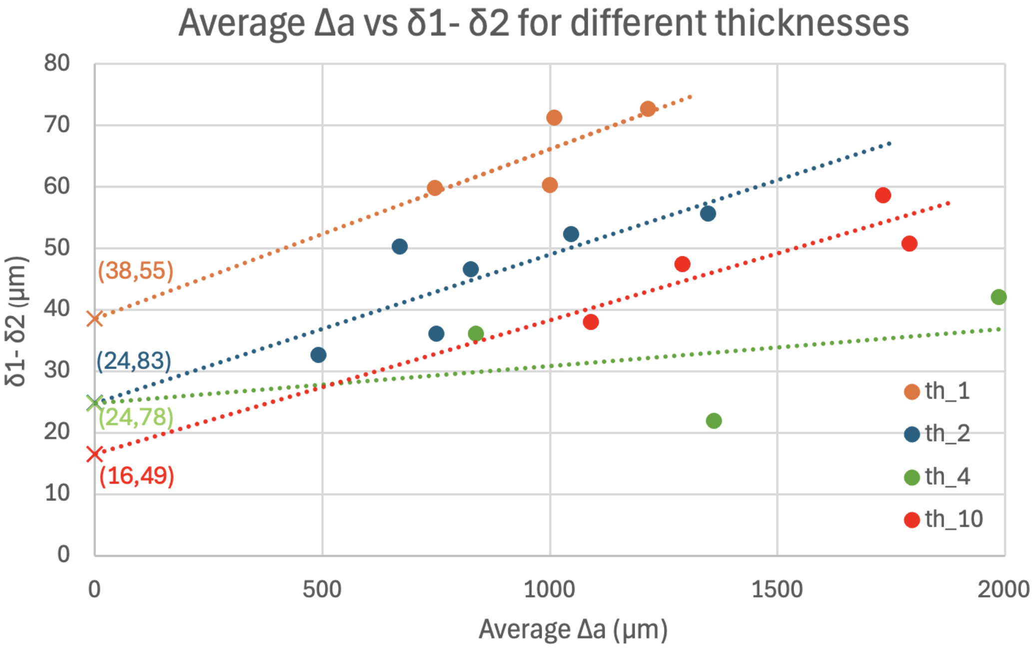

Figure 4.4.6: δ_1-δ_2 as a function of Δa

As expected, the results show a clear dependence on specimen thickness. The critical CTOD is significantly higher in thinner samples and decreases with increasing thickness. This trend reflects the transition in stress state: thin specimens are dominated by plane stress conditions, which allow for more plastic deformation and higher apparent toughness, while thicker specimens are increasingly governed by plane strain conditions, where the constraint on plastic flow near the crack tip reduces the CTOD. The values of δ_c obtained from the linear regression for each thickness are reported in Table 4.4.1. It is worth noting that although the CTOD value obtained for the 4 mm specimens appears consistent with the trend, the reliability of this result is limited. Several samples of this thickness failed prematurely during the pre-cracking and tensile test phases, resulting in an insufficient number of valid data points to ensure statistical robustness. Therefore, the 4 mm value should be interpreted with caution.

Thickness [mm]	**Critical CTOD δ_c [µm]**
1	38.55
2	24.83
4	24.78
10	16.49

Table 4.4.1: Critical CTOD δ_c values for each specimen thickness, obtained by linear regression at $\Delta a = 0$

These differences in crack morphology through the thickness provide experimental validation of the stress state transition from plane stress (surface) to plane strain (midplane) conditions. The tomography data particularly confirms that the apparent higher toughness at surfaces arises from reduced constraint, allowing greater plastic deformation and slower crack advancement compared to the highly constrained central region.

4.4.1 Destructive Through-Thickness Crack Characterization via Stepwise Polishing

In addition to the non-destructive characterization performed through X-ray Computed Tomography (CT), an alternative destructive technique was employed to assess the crack morphology through the thickness of selected specimens. This method was based on sequential material removal (polishing) and optical measurement of the surface crack profile at different thickness levels.

The procedure was applied to two DENT specimens, one with an initial thickness of 10 mm and another of 4 mm. Both samples had been previously tested and fractured during CTOD experiments. After testing, the crack was first examined at the surface using a 3D optical microscope to measure the initial crack opening and length at the original surface.

Following this initial measurement, the specimen was polished using a grinding machine equipped with P80-grade abrasive paper. The goal was to remove material from the specimen surface at each polishing step. After each polishing pass, the sample was cleaned and again analyzed under the 3D optical microscope to document the evolution of the crack along the newly exposed surface. This process was repeated until the full through-thickness crack path was revealed.

In total, about ten intermediate measurements were acquired for each sample. The results allowed the reconstruction of the crack morphology along the thickness using independent surface observations, providing a stepwise mapping of the crack length as a function of depth.

Then a comparison with the tomography-based results was performed, showed in Figure 4.4.7 and 4.4.8, revealing an excellent agreement between the two methods. Despite the inherently destructive nature of the polishing-based technique, the correlation confirmed the reliability of the CT scans and validated the 3D imaging of crack tunneling and progression.

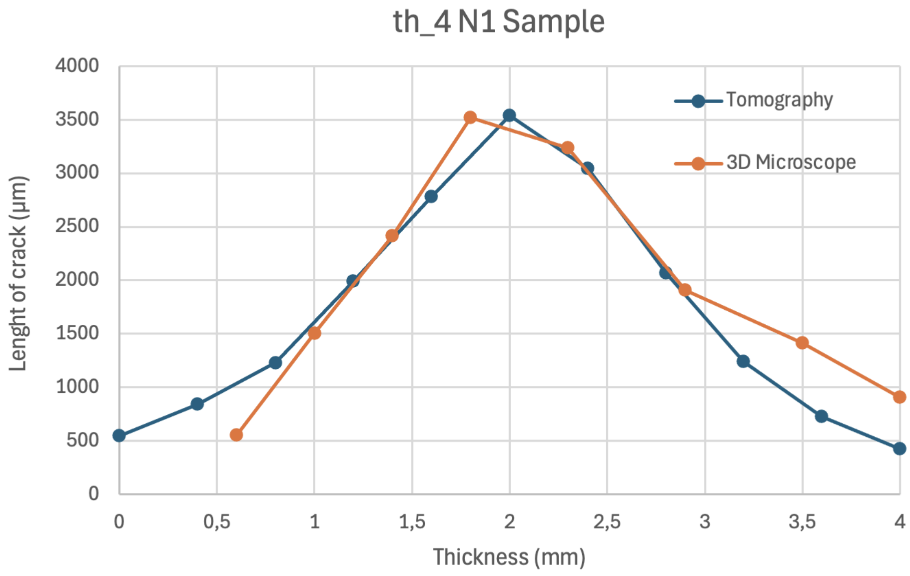

Figure 4.4.7: Comparison between crack length measured with tomography and polishing + 3D microscope for the same 4 mm sample

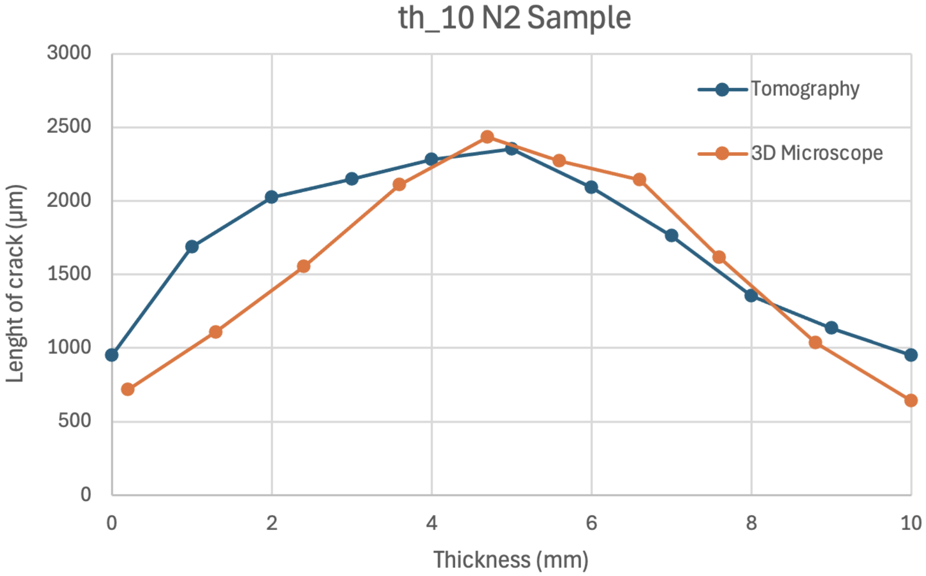

Figure 4.4.8: Comparison between crack length measured with tomography and polishing + 3D microscope for the same 10 mm sample

This stepwise destructive approach offers an alternative validation tool for assessing internal damage evolution, particularly in research environments where access to high-resolution tomography equipment may be limited. Moreover, it provides an intuitive and direct visualization of crack front evolution, which can be valuable for educational and verification purposes.

Chapter 5

Conclusions

This master's thesis investigated the fracture resistance of Al2050 alloy through an experimental campaign focusing on thickness-dependent fracture toughness using Crack Tip Opening Displacement (CTOD) methodology. The study employed Double Edge Notched Tensile (DENT) specimens across four thicknesses (1mm, 2mm, 4mm, and 10mm) to examine the transition from plane stress to plane strain conditions. The key findings and implications are summarized as follows:

- **Thickness-Dependent Fracture Toughness:** Experimental results demonstrated a clear thickness dependence of fracture resistance, with thinner specimens (1mm) exhibiting significantly higher critical CTOD values (38.55µm) compared to thicker specimens (10mm, 16.49µm). This confirms that plane stress conditions in thin sheets promote greater plastic deformation and energy absorption during fracture.
- **Fracture Surface Morphology:** Fractographic analysis revealed distinct failure mechanisms across thicknesses:
  - Thin specimens (1mm) showed complete slant fracture surfaces (45°), characteristic of shear-dominated plane stress conditions
  - Thick specimens (10mm) exhibited mixed-mode fracture with flat central regions (plane strain) and slanted surfaces (plane stress), demonstrating through-thickness constraint variations
- **Crack Tunneling Phenomenon:** X-ray tomography and destructive polishing techniques both confirmed crack tunneling behavior in thicker specimens, where the crack front advanced faster at mid-thickness due to higher triaxial constraint. This validates the theoretical framework of thickness-dependent stress states.
- **Material microstructure and anisotropy**: Microstructural characterization revealed a reasonably homogeneous distribution through thickness, although localized inhomogeneities and second-phase particles were detected, particularly near the mid-thickness of thicker specimens. These may have contributed to local damage initiation and variability in fracture response.
- **Material Condition Comparison:** While the main experimental campaign was conducted on Al2050-T8, preliminary T3 characterization revealed:

  - Higher ductility in T3 condition (true fracture strain 0.193 vs T8's 0.12)
  - Anisotropic behavior with 8-15% variation in mechanical properties between rolling and transverse directions
  - Microstructural differences in precipitate distribution affecting crack initiation

- **Experimental Methodology Validation:** The excellent correlation between non-destructive (X-ray tomography) and destructive (stepwise polishing) crack length measurements confirmed the reliability of the experimental approach for through-thickness fracture characterization.

- **Thickness Optimization:** The results suggest an optimal thickness range (1-2mm for Al2050-T8) where fracture toughness peaks before decreasing toward plane strain values, providing practical guidelines for lightweight structural design in aerospace applications.

Future research directions emerging from this work include:

- Extension of thickness range testing to identify the precise thickness where fracture toughness peaks for Al2050 alloys

- Investigation of temper effects through comparative CTOD studies on T3 vs T8 conditions to quantify heat treatment influences on thickness dependence

- Development of thickness-dependent fracture criteria incorporating both CTOD and Essential Work of Fracture (EWF) approaches

- Microstructural studies correlating grain orientation and precipitate distribution with through-thickness crack propagation

- Integration of experimental results with computational models to predict fracture behavior in multi-thickness components

Overall, this work contributes to the understanding of fracture behavior in lightweight aluminum alloys and provides experimental validation for the role of thickness in ductile fracture. The methods and insights developed here offer a valuable foundation for future investigations and applications in damage-tolerant design.

Bibliography

[1] A. Nouri, A. Rohani, Y. Li, and C. Wen, "Biodegradable metallic suture anchors: A review," *Smart Materials in Manufacturing*, vol. 1, June 2022.

[2] W. contributors, "Stress concentration." https://en.wikipedia.org/wiki/Stress_concentration, 2023.

[3] H. L. Ewalds and R. J. H. Wanhill, *Fracture Mechanics*. Edward Arnold and Delftse Uitgevers Maatschappij, 1984.

[4] Ultmeche, "Stress-strain curve," 2024.

[5] A. Subhy, "Advanced analytical techniques in fatigue and rutting related characterisations of modified bitumen: Literature review," *Construction and Building Materials*, 2017.

[6] J. Han, S. Matsubara, S. Moriguchi, and K. Terada, "Variational crack phase-field model for ductile fracture with elastic and plastic damage variables," *Computer Methods in Applied Mechanics and Engineering*, 2022.

[7] H. E. Bhilat and H. Abdelilah, "Experimental and numerical investigation of the influence of temperature on the fracture behavior of high impact polystyrene evaluated by the j-integral approach using multiple specimen method," *Journal of Metals Materials and Minerals*, vol. 30, September 2020.

[8] AFGROW, "Dtd handbook: Handbook for damage tolerant design," 2023.

[9] Y. Chen and J. Yang, "Small-strain shear modulus of silty sands: the role of sample preparation method," *Geotechnique*, vol. 74, pp. 367–382, December 2023. Publisher preview available.

[10] Xometry, "Hardness testing of metals: Methods and comparisons," 2023.

[11] T. Pardoen and F. Delannay, "A method for the metallographical measurement of the ctod at cracking initiation and the role of reverse plasticity on unloading," 2000.

[12] A. Riaz, G. Hussain, U. Naveed, W. Hongyu, M. Alkahtani, and M. Khan, "An investigation on the effects of tool rotational speed and material temper on post-isf tensile properties of Al2219 alloy," *Journal of Materials Research and Technology*, vol. 10, 2020.

[13] M. F. Ashby, “Material property charts,” in *Materials Selection in Mechanical Design*, Butterworth-Heinemann, 2011.

[14] T. L. Anderson, *Fracture Mechanics: Fundamentals and Applications.* CRC Press, 2005.

[15] T. H. Courtney, *Mechanical Behavior of Materials.* McGraw-Hill, 2005.

[16] D. Broek, *Elementary Engineering Fracture Mechanics.* Springer, 1982.

[17] T. Mura, *Micromechanics of Defects in Solids.* Springer, 1987.

[18] R. E. Peterson, *Stress Concentration Factors.* John Wiley & Sons, 1974.

[19] J. Schijve, *Fatigue of Structures and Materials.* Springer Science Business Media, 2009.

[20] J. R. Rice, “A path independent integral and the approximate analysis of strain concentration by notches and cracks,” *Journal of Applied Mechanics*, vol. 35, no. 2, pp. 379–386, 1968.

[21] A. A. Griffith, “The phenomena of rupture and flow in solids,” *Philosophical Transactions of the Royal Society of London. Series A*, vol. 221, pp. 163–198, 1921.

[22] G. R. Irwin, “Analysis of stresses and strains near the end of a crack traversing a plate,” *Journal of Applied Mechanics*, vol. 24, pp. 361–364, 1957.

[23] A. A. Griffith, *The Phenomena of Rupture and Flow in Solids.* Cambridge University Press, 1921.

[24] G. R. Irwin, *Fracture Mechanics.* McGraw-Hill, 1957.

[25] E. Orowan, *Fracture and Strength of Solids.* Oxford University Press, 1948.

[26] T. L. Anderson, *Fracture Mechanics: Fundamentals and Applications.* CRC Press, 2017.

[27] S. Timoshenko and J. Goodier, *Theory of Elasticity.* McGraw-Hill, 1970.

[28] D. Broek, *Elementary Engineering Fracture Mechanics.* Springer, 1983.

[29] N. Petch, “The cleavage strength of polycrystals,” *Journal of the Iron and Steel Institute*, vol. 174, pp. 25–28, 1953.

[30] J. H. Hollomon, “Tensile deformation,” *Transactions of the AIME*, vol. 162, pp. 268–290, 1945.

[31] W. D. C. Jr. and D. G. Rethwisch, *Fundamentals of Materials Science and Engineering: An Integrated Approach.* Wiley, 8 ed., 2010.

[32] Wikipedia contributors, “Stress triaxiality — wikipedia, the free encyclopedia.” `https://en.wikipedia.org/wiki/Stress_triaxiality`, 2023.

[33] J. W. Hancock and A. C. Mackenzie, "On the mechanisms of ductile failure in high-strength steels subjected to multi-axial stress-states," *Journal of the Mechanics and Physics of Solids*, vol. 24, no. 2, pp. 147–169, 1976.

[34] J. L. H. R. W. Hertzberg, R. P. Vinci, *Deformation and Fracture Mechanics of Engineering Materials.* John Wiley & Sons, 2012.

[35] J. R. Rice, "A path independent integral and the approximate analysis of strain concentration by notches and cracks," *Journal of Applied Mechanics*, vol. 35, pp. 379–386, 1968.

[36] A. A. Wells, "Unstable crack propagation in metals: Cleavage and fast fracture," *Proceedings of the Crack Propagation Symposium*, vol. 1, pp. 210–230, 1961.

[37] C. F. Shih, "Relationships between the J-integral and the crack opening displacement for stationary and extending cracks," *Journal of the Mechanics and Physics of Solids*, vol. 29, no. 4, pp. 305–326, 1981.

[38] R. M. McMeeking, "Finite deformation analysis of crack-tip opening in elastic-plastic materials and implications for fracture," *Journal of the Mechanics and Physics of Solids*, vol. 25, no. 5, 1977.

[39] W. Lan, X. Deng, and M. A. Sutton, "Investigation of crack tunneling in ductile materials," *Engineering Fracture Mechanics*, vol. 77, no. 14, 2010.

[40] J. W. Hutchinson, "Singular behaviour at the end of a tensile crack in a hardening material," *Journal of the Mechanics and Physics of Solids*, vol. 16, pp. 13–31, 1968.

[41] T. Pardoen, Y. Marchal, and F. Delannay, "Essential work of fracture compared to fracture mechanics—towards a thickness independent plane stress toughness," *Engineering Fracture Mechanics*, vol. 69, no. 5, pp. 617–631, 2002.

[42] A. C. Kak and M. Slaney, *Principles of Computerized Tomographic Imaging.* Philadelphia, PA: SIAM, classics in applied mathematics ed., 2001.

[43] S. R. Stock, *Microcomputed Tomography: Methodology and Applications.* Boca Raton, FL: CRC Press, 2008.

[44] E. Maire and P. J. Withers, "Quantitative X-ray Tomography," *International Materials Reviews*, vol. 59, no. 1, p. 1–43, 2014.

[45] G. N. Hounsfield, "Computed Medical Imaging," *British Journal of Radiology*, vol. 46, no. 552, p. 1016–1022, 1973.

[46] S. C. Garcea, P. J. Withers, and I. Sinclair, "In-situ 3d x-ray imaging of fracture damage in al–si alloys under load," *Materials Science and Engineering A*, vol. 719, p. 1–10, 2018.

[47] J. R. Davis, *Aluminum and Aluminum Alloys.* ASM International, 1993.

[48] G. F. V. Voort, *Metallography: Principles and Practice.* ASM International, 1999.

[49] S. Javangorouh, "A contribution to the study of crack initiation in metal plates," 2024. Master Thesis, Ecole Polytechnique de Louvain. Supervisors: Thomas Pardoen.

[50] R. Rioja and J. Liu, "Metallurgy of aluminum-lithium alloys," *Materials Science Forum*, vol. 706, pp. 3–14, 2012.

[51] W. Contributors, "Bauschinger effect." `https://en.wikipedia.org/wiki/Bauschinger_effect`, 2023.

[52] Z. Zhang and M. Hauge, "Experimental characterization of cyclic plasticity in thin aluminum sheets," *International Journal of Fatigue*, vol. 24, no. 2, pp. 183–191, 2002. Analisi sperimentale dell'isteresi in Al2024 e Al7075.

Appendix A

Preliminary CTOD Tests on Al2050-T3

This appendix contains preliminary experimental data from CTOD tests performed on Al2050-T3 specimens. These tests were carried out before switching to the Al2050-T8 condition. Although the results are not used in the final fracture assessment, they are included here for completeness and to provide potential insight for future studies.

A.1 Crack Tip Opening Displacement (CTOD) Experiments on Al2050 T-3 Alloy

This section describes the experimental procedures and results for Crack Tip Opening Displacement (CTOD) testing conducted on the Al2050 T-3 alloy. Unlike the previous investigation on Al2050 T-8 alloy which considered four different thicknesses (1, 2, 4, and 10 mm), the current study focuses on three specimen thicknesses: **1 mm, 2 mm**, and **4 mm**, with the detailed geometry illustrated in Figure A.1.1.

The reduced thickness range was selected because preliminary studies indicated that the critical **thickness peak**, where the transition between plane stress and plane strain conditions occurs, falls below 4 mm for this material. Testing a 10 mm thick specimen was deemed unnecessary since such thickness lies well beyond the plane strain dominance region, and our primary interest lies in identifying the thickness-dependent fracture behavior near the transition zone.

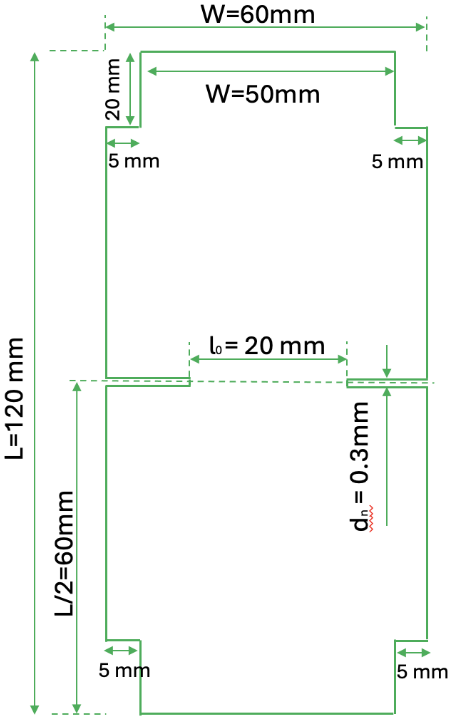

Figure A.1.1: Geometry of the Al2050 T-3 specimen

A.1.1 Fatigue Pre-Cracking

The procedure begins, as already done for the T-8 alloy, with fatigue precracking of double edge notched tension (DENT) specimens to generate sharp crack tips prior to the main interrupted tensile tests.

The multiple specimen approach used in this study allows the simultaneous determination of both CTOD at crack initiation and J-integral values for each specimen. A detailed description of the measurement techniques and experimental protocols is provided, providing complete documentation of the testing methodology.

Sample	Average Load (N)	Number of cycles	Frequency (Hz)
1	5,585	41,000	30
2	6,071	28,000	30
3	6,800	30,000	30
4	6,533	30,000	30
5	6,588	34,000	30

Table A.1.1: atigue pre-cracking parameters for 4 mm specimens

The average load for each sample was computed using a **cycle-weighted mean** to properly account for the contribution of each load step. The formula is given by:

$$\bar{F} = \frac{\sum_{i=1}^{n} (N_i \times F_i)}{\sum_{i=1}^{n} N_i}$$

where N_i is the number of cycles at load F_i. This approach provides a more accurate representation of the actual loading history than a simple arithmetic mean, as it weights each load level by its corresponding number of cycles. The incremental load strategy (progressing from lower to higher forces) was essential to determine the optimal load range for crack initiation: initial lower loads (4,200–5,000 N) promoted controlled crack nucleation, while subsequent higher loads (up to 8,000 N) enabled stable crack propagation. This methodology minimized the risk of either insufficient crack growth or excessive plastic deformation.

The same fatigue pre-cracking procedure was subsequently applied to specimens with reduced thicknesses of 2 mm and 1 mm. For the 2 mm samples, a slightly lower initial load range was adopted to account for the reduced cross-sectional area, while maintaining the same loading frequency of 30 Hz. The pre-cracking strategy remained based on incrementally applied loads to ensure stable crack growth without premature plastic deformation. The experimental results for the 2 mm specimens are summarized in Table A.1.2.

Sample	**Average Load (N)**	**Number of cycles**	**Frequency (Hz)**
1	4,500	10,000	30
2	5,000	10,000	30
3	5,000	12,000	30
4	5,000	12,000	30
5	5,000	12,000	30

Table A.1.2: Fatigue pre-cracking parameters for 2 mm specimens

For the 1 mm thick specimens, the loading frequency was reduced to 20 Hz to minimize thermal effects and dynamic amplification, which become more critical at lower thicknesses. Initially, a pre-cracking load of 4,000 N was applied to Sample 1; however, the specimen failed prematurely after 9,000 cycles, indicating that the applied load was excessive for this thickness. As a result, the maximum load was reduced in the following tests to avoid unintended fracture before completing the fatigue pre-cracking stage.

Unfortunately, due to surface damage and irregular notch geometry in the 1 mm samples, accurate crack opening and ligament length measurements using the 3D digital microscope were not possible. Despite successful completion of fatigue pre-cracking on some specimens, the crack tips could not be clearly resolved on both sides of the notch, making CTOD analysis unreliable. Consequently, the 1 mm samples were excluded from further analysis, and the experimental campaign on this thickness was discontinued. The defective specimens were returned to the supplier for quality verification, and no fracture toughness testing was performed on this configuration.

Only the 2 mm and 4 mm specimens are included in the following dimensional and CTOD evaluations.

Sample	Average Load (N)	Number of cycles	Frequency (Hz)
1	4,000	9,000	20
2	3,000	12,000	20
3	3,400	10,000	20
4	3,400	10,000	20
5	3,400	10,000	20

Table A.1.3: Fatigue pre-cracking parameters for 1 mm specimens

This tailored approach to fatigue pre-cracking ensured the formation of sharp and stable cracks across all thickness configurations. Adjusting load levels and frequency based on specimen geometry was essential to achieve repeatable crack growth behavior, minimize scatter in initial crack lengths, and avoid premature failure. The resulting cracks provide a consistent starting point for subsequent quasi-static tests aimed at quantifying fracture resistance parameters such as CTOD and J-integral.

Following the fatigue pre-cracking, all samples were measured with a 3D microscope. As already in the case of the T-8 samples, each parameter was measured on both sides of the notch for the five samples in each thickness group. The values in Table **??** show the average of these measurements (ten per thickness, combining the two sides of five samples). The ligament size after pre-cracking was calculated using the same averaging method.

Sample with thickness 2 mm	
Opening of notch	0.373 mm
Notch radius	0.182 mm
Pre-crack length	0.728 mm
Initial ligament distance	19.92 mm
Ligament size after precracking	18.47 mm

Table A.1.4: Averaged dimensions of the 2 mm T-3 samples after fatigue pre-cracking

Sample with thickness 4 mm	
Opening of notch	0.372 mm
Notch radius	0.180 mm
Pre-crack length	0.379 mm
Initial ligament distance	19.93 mm
Ligament size after precracking	19.17 mm

Table A.1.5: Averaged dimensions of the 4 mm T-3 samples after fatigue pre-cracking

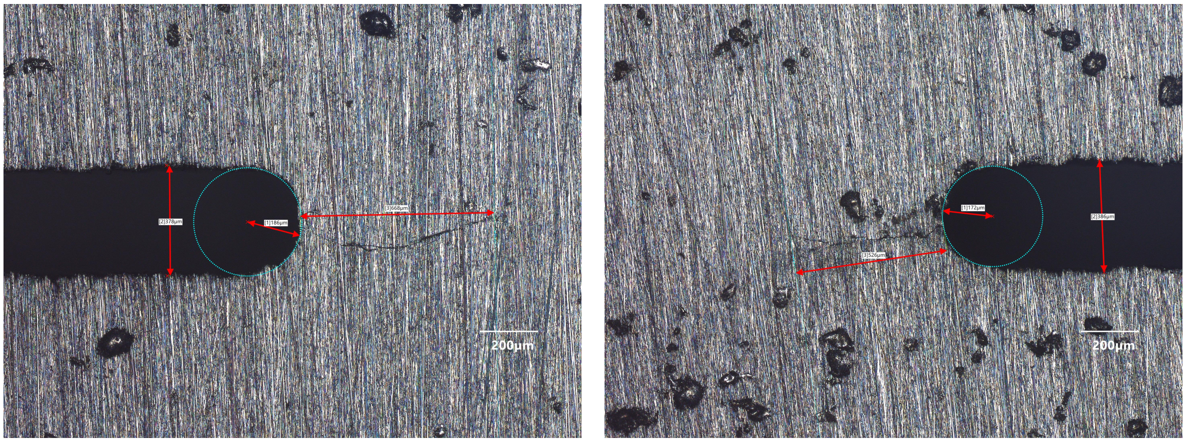

(a) Left crack measurement (b) Right crack measurement

(c) Ligament distance measurement

Figure A.1.2: 3D microscope images showing crack features for 2 mm thick sample

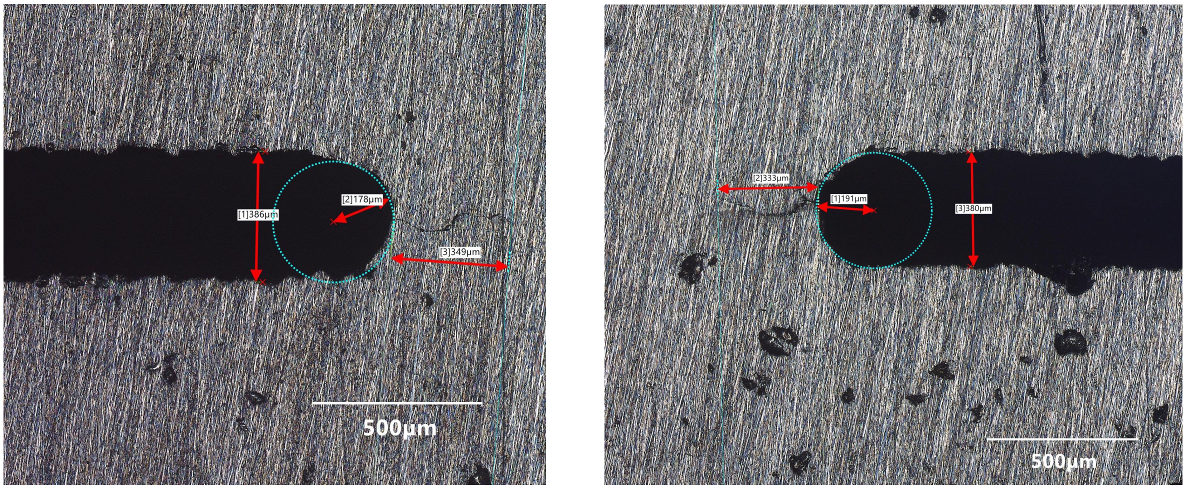

(a) Left crack measurement

(b) Right crack measurement

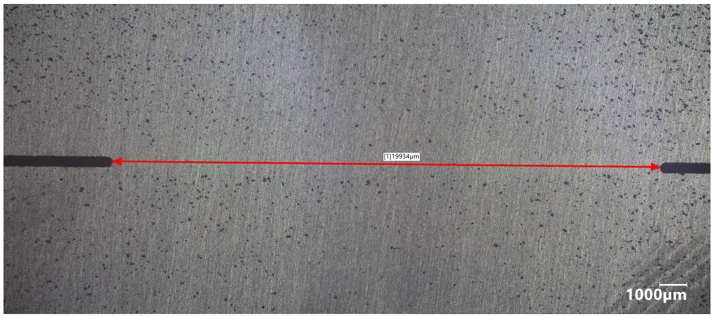

(c) Ligament distance measurement

Figure A.1.3: 3D microscope images showing crack features for 4 mm thick sample